Enderle, U., Mechie, J., Sobolev, S. V., Fuchs, K. (1996): Seismic anisotropy within the uppermost mantle of southern Germany. - Geophysical Journal International, 125, 3, pp. 747—767.

DOI: http://doi.org/10.1111/j.1365-246X.1996.tb06021.x

Geophys. J. Int. (1996) **125**, 747–767

Seismic anisotropy within the uppermost mantle of southern Germany

U. Enderle,[1] J. Mechie,[2] S. Sobolev[1,3] and K. Fuchs[1]

[1] *Geophysical Institute, University of Karlsruhe, Hertzstrasse* 16, D-76187 *Karlsruhe, Germany*
[2] *GeoForschungsZentrum Potsdam, Telegrafenberg* A3, D-14473 *Potsdam, Germany*
[3] *Institute of Physics of the Earth, Moscow, Russia*

Accepted 1996 January 19. Received 1996 January 18; in original form 1995 January 4

SUMMARY

This paper presents an updated interpretation of seismic anisotropy within the uppermost mantle of southern Germany. The dense network of reversed and crossing refraction profiles in this area made it possible to observe almost 900 traveltimes of the P_n phase that could be effectively used in a time-term analysis to determine horizontal velocity distribution immediately below the Moho. For 12 crossing profiles, amplitude ratios of the P_n phase compared to the dominant crustal phase were utilized to resolve azimuthally dependent velocity gradients with depth. A *P*-wave anisotropy of 3–4 per cent in a horizontal plane immediately below the Moho at a depth of 30 km, increasing to 11 per cent at a depth of 40 km, was determined. For the axis of the highest velocity of about 8.03 km s^{-1} at a depth of 30 km a direction of N31°E was obtained. The azimuthal dependence of the observed P_n amplitude is explained by an azimuth-dependent sub-Moho velocity gradient decreasing from 0.06 s^{-1} in the fast direction to 0 s^{-1} in the slow direction of horizontal *P*-wave velocity. From the seismic results in this study a petrological model suggesting a change of modal composition and percentage of oriented olivine with depth was derived.

Key words: anisotropy, Germany, seismic refraction, upper mantle.

1 INTRODUCTION

Regional *P*-wave seismic models for the uppermost mantle layer beneath south-west Germany based on time-term analysis were published by Bamford (1973, 1976a, 1976b, 1977). These models all feature around 7 per cent anisotropy involving azimuthally dependent velocities, with the direction of fast velocity at about N22°E. Fuchs (1983) used these results, together with qualitative observations of the distribution of P_n amplitudes with azimuth and the velocity–depth function from the seismic profiles SB-060 and 09-240 beneath south-west Germany, to continue the anisotropic model to greater depth. This resulted in the so-called *anvil* model. Fuchs (1983) further interpreted this seismic model in terms of petrological composition.

Since the time-term analysis of Bamford, recent explosion seismic experiments have provided additional P_n observations. In this paper, first these observations are included in a new time-term analysis of the P_n data from south-west Germany using the Bamford (1977) formulation. Further, the data are analysed for lateral inhomogeneity based on the extended time-term method developed by Hearn (1984). In order to continue the time-term model to greater depth, the azimuthally dependent velocity gradient in the uppermost mantle layer is determined. As amplitudes are more sensitive to velocity gradients than traveltimes, this is accomplished by quantitatively analysing P_n amplitudes from 12 azimuthally distributed profiles in a 250 × 300 km area in the south-west German triangle. The band method, which facilitates the comparison between observed amplitude-ratio curves and a range of theoretical curves, is used for quantitatively analysing P_n amplitudes. The derived sub-Moho velocity gradients are then taken into account by extending the time-term method for media with azimuthally dependent velocity gradients. This gives the possibility of combining traveltime and amplitude information in a single inversion process.

From the improved seismic model, in which the amount of anisotropy immediately below the Moho is about half that of previous models, and the velocity in the fast direction is about 0.3 km s^{-1} smaller than in previous models (e.g. Bamford 1977), a petrological model is derived and the uppermost mantle layer of the anvil model is thus revised.

2 THEORY OF TIME-TERM ANALYSIS

The purpose of the time-term analysis in this study is to provide the essential features of Moho topography and

uppermost mantle velocity, including regional anisotropy and lateral heterogeneity, immediately below the Moho. The time-term analysis is applied to the data set of 882 first arrivals from the network of reversed and crossing seismic profiles in south-west Germany. For this amount of data from reversed and crossing profiles, the time-term method is particularly effective.

The time-term method is well known as an inversion of observed traveltime data from refracted waves in a 3-D model with the opportunity for statistical evaluation. The theory of the time-term method for the case of a constant velocity refractor was described in detail by Willmore & Bancroft (1960) and Berry & West (1966). Raitt *et al.* (1969) and Bamford (1973) extended the theory to include azimuthal variation of refractor velocity, based on the formula of Backus (1965) for weak anisotropy. The next significant step in the development of the method was the introduction of the *mosaic* concept by Bamford (1976a). For this method individual shots and/or stations are grouped together into mosaics of arbitrary shape and size, thus a solution that sufficiently accounts for the variation in refractor topography, but which is at the same time stable, can be obtained. Finally, Hearn (1984) developed the method to include lateral variation of refractor velocity with or without the presence of a regionally constant anisotropy. This was accomplished by dividing the area to be analysed into a number of rectangular blocks with varying edge lengths.

Following Hearn (1984), the traveltime t_k for a refracted wave between sites i and j is (see also Fig. 1)

$$t_k = a_i(v_p) + a_j(v_q) + \sum_{l=1}^{n} \frac{D_{kl}}{v_l}, \tag{1}$$

where v_p and v_q are the velocities in blocks p and q, which the ray enters and leaves, respectively. D_{kl} is the distance that the refracted ray travels in block l with velocity v_l, and n is the number of blocks. Eq. (1) shows that the time terms depend on the velocities of the individual blocks. Graphically the time term a_i represents the time that a seismic ray will take to travel from site i down to the refractor, minus the traveltime that the ray would take to travel the offset distance F_i (Fig. 1) within the refractor. The definition of a_j is analogous. In order to facilitate a comparison between the time terms for the various sites, it is necessary to calculate them with respect to a mean refractor velocity, v_m. This can be achieved by a first-order Taylor series expansion of eq. (1), which gives

$$t_k = a_i(v_m) + a_j(v_m) + \sum_{l=1}^{n} \frac{D_{kl}}{v_m} + \left(\frac{\partial a_i}{\partial v}\right)_{v=v_m} \delta v_m^{(p)} + \left(\frac{\partial a_j}{\partial v}\right)_{v=v_m} \delta v_m^{(q)} - \sum_{l=1}^{n} \frac{D_{kl}}{v_m^2} \delta v_m^{(l)}, \tag{2}$$

where $\delta v_m^{(l)}$ is the velocity variation with respect to v_m for block l. The correction term $\Sigma\, D_{kl}/v_m^2 \delta v_m^{(l)}$ for the mean velocity disappears when each block is assigned its own velocity v_l. The time term a_i can be expressed as a function of the mean refractor velocity v_m and the velocity–depth function $v(z_i)$ above the refractor and perpendicular to the surface at site i (see Berry & West 1966, eq. 1-1). With $(\partial a_i/\partial v)_{v=v_m} = F_i/v^2$, eq. (2) becomes

$$t_k = a_i(v_m) + a_j(v_m) + \sum_{l=1}^{n} \frac{D_{kl}}{v_l} + \frac{1}{v_m^2}(F_i \delta v_m^{(p)} + F_j \delta v_m^{(q)}). \tag{3}$$

Including a regionally constant anisotropy in the model, the refractor velocity is given by a superposition of the horizontal velocity variation, $\delta v_m^{(l)}$, the azimuthal velocity variation, $\delta v_m(\theta)$, and the mean refractor velocity,

$$v(l, \theta) = v_m + \delta v_m^{(l)} + \delta v_m(\theta), \tag{4}$$

where θ is the azimuth and, for weak anisotropy (Backus 1965),

$$\delta v_m(\theta) = A \sin 2\theta + B \cos 2\theta + C \sin 4\theta + D \cos 4\theta. \tag{5}$$

Following Bamford (1973), and once again using a first-order Taylor series expansion for the traveltime, t_k, gives

$$t_k = a_i + a_j + \sum_{l=1}^{n} \frac{D_{kl}}{v_l} + \frac{1}{v_m^2} \times \left[F_i \delta v_m^{(p)} + F_j \delta v_m^{(q)} + \left(F_i + F_j - \sum_{l=1}^{n} D_{kl} \right) \delta v_m(\theta) \right]. \tag{6}$$

In order to overcome the problem that F_i and $F_i \delta v_m^{(l)}$ are unknown, eq. (6) is solved iteratively by least squares until no significant change (100 m in the case of F_i; 0.01 s in the case

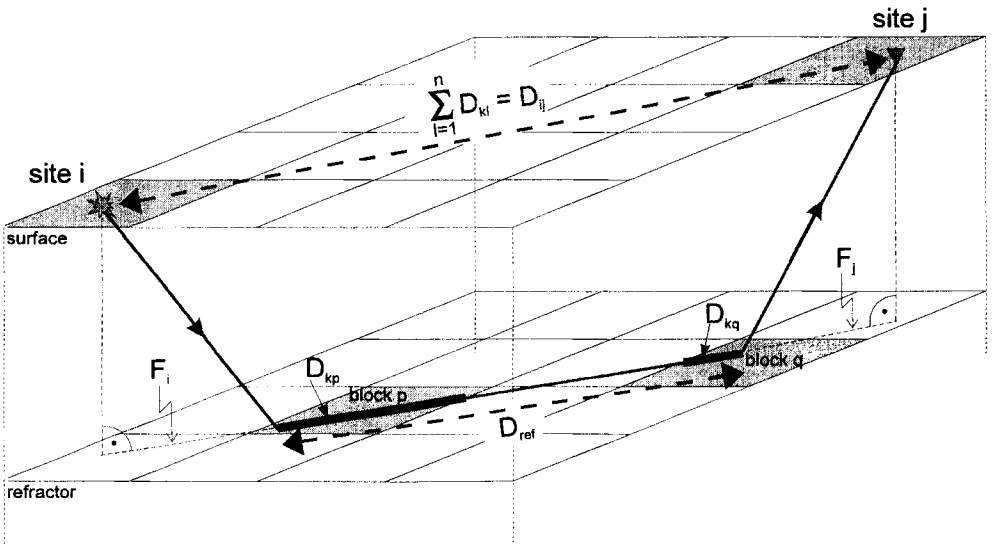

Figure 1. Sketch of ray path through a block model.

of $F_i \delta v_m^{(l)}$) in these quantities occurs from one iteration to the next. This procedure is different from that of Bamford (1973, 1976a, 1977) and Hearn (1984), who performed no iterations and used a constant-offset value in their initial solutions. In this study, F_i was initially set to 30 km and $\delta v_m^{(l)}$ to zero. For the data sets considered here, three to four iterations were usually necessary to obtain convergence. The influence of the average crustal velocity required to calculate F_i will be discussed below. As noted by Hearn (1984), when the refractor is divided into blocks for the determination of lateral heterogeneity, it is sometimes necessary to damp that part of the solution that solves for the horizontal velocity variation.

The time-term analysis described above is only valid for a vertically homogeneous refractor. As the P_n phase is often observed with much higher amplitudes than a pure headwave could produce, the time-term method has been extended for diving waves. To allow also for an increase of anisotropy with depth, an azimuthal variation of P_n velocity gradient with depth has been included in the analysis for a laterally homogeneous medium and the case of anisotropy with 2θ terms only. This extension makes it possible to combine traveltime and amplitude information of P_n to estimate a least-squares refractor velocity for each depth within the velocity gradient layer. It will be shown that this combination gives a noticeable effect compared to previous solutions.

Combining the traveltime information with the knowledge of the maximum and minimum velocity gradient derived from first amplitude modelling steps (e.g. Section 4) enables the azimuthal distribution of the velocity at the base of the

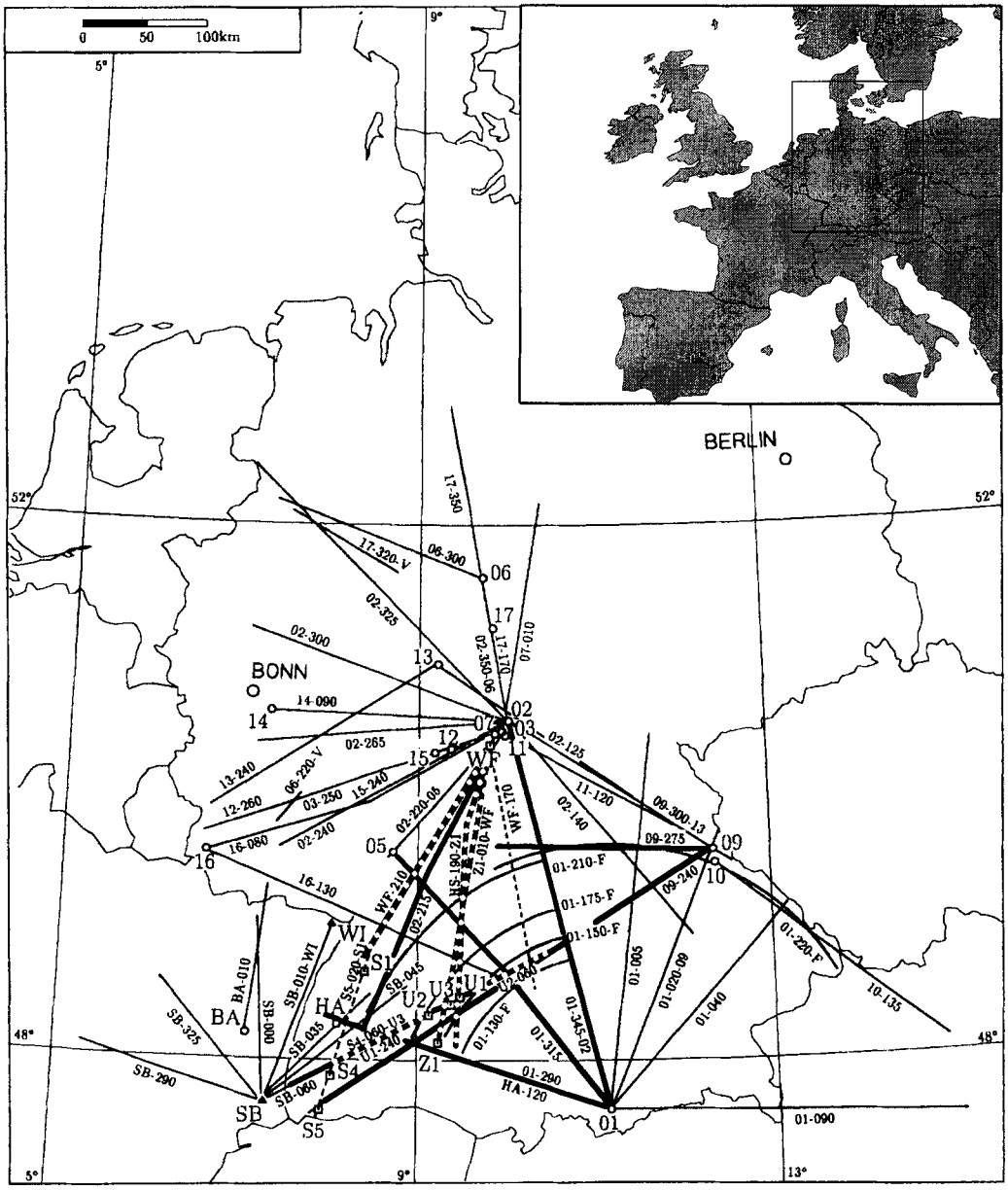

Figure 2. Seismic refraction profiles in southern Germany which provide P_n traveltime data for this study. Profiles providing new P_n data are shown as dashed lines. Profiles shown as thick lines (solid or dashed) are used for amplitude analysis. The notation of profiles is as follows: shot ID–azimuth of profile–reverse shot ID (if it exists).

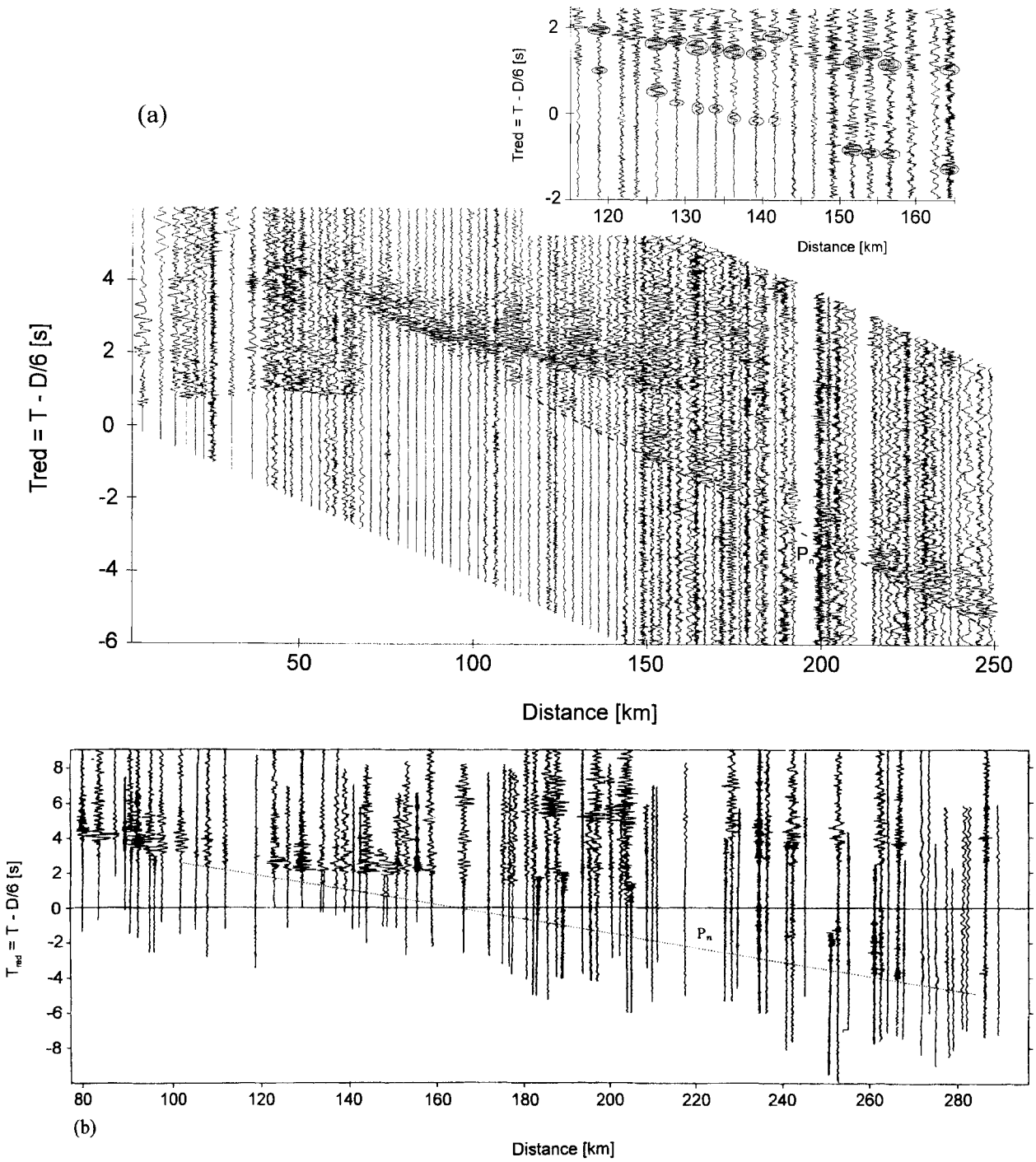

Figure 3. Two record section examples for P_n data. Note that the P_n phase is clearly visible in (a) profile Z1-010-WF (azimuth: 10°) but is difficult to trace in (b) profile 01-315 (azimuth: 315°). In addition to the traveltime correlation shown in both record sections as a least-squares straight-line fit, examples of the peak-to-peak amplitudes of the P_n phase and the dominant crustal phase are also marked for the profile Z1-010-WF. Both record sections are plotted trace-normalized with a reduction velocity of 6.0 km s^{-1}.

refractor to be determined. The thickness of the refracting layer is assumed to be known from preliminary traveltime and amplitude modelling. With the azimuthal velocity distribution at the top and bottom of the refracting layer now known, the azimuthal distribution of the velocity gradient k ($k > 0$) can be determined:

$$k(\theta) = \frac{\partial v_m(\theta)}{\partial z} = \frac{(v_m^{bottom} - v_m^{top}) + (A^{bottom} - A^{top}) \sin 2\theta + (B^{bottom} - B^{top}) \cos 2\theta}{z^{bottom} - z^{top}}. \quad (7)$$

The traveltime in the refracting layer, t_{ref}, can now be approximated by (see e.g. Dobrin 1976)

$$t_{ref}(\theta) = \frac{2}{k(\theta)} \sinh^{-1} \frac{k(\theta) D_{ref}}{2v^{top}(\theta)}, \quad (8)$$

where

$$D_{ref} = \sum_{l=1}^{n} D_{kl} - F_i - F_j$$

is the horizontal distance travelled by the ray in the refracting layer. The effective or average velocity in the refracting layer is thus

$$v = \frac{D_{ref}}{t_{ref}}. \quad (9)$$

If the ray reaches the bottom of the velocity gradient layer and the horizontal distance travelled, D^*, is smaller than D_{ref}, then it is assumed that the velocity $v^{bottom}(\theta)$ continues to greater depth, and

$$t_{ref}(\theta) = \frac{2}{k(\theta)} \sinh^{-1} \frac{k(\theta) D^*}{2v^{top}(\theta)} + \frac{D_{ref} - D^*}{v^{bottom}(\theta)}, \quad (10)$$

where $D^* = 0.5k(\theta)\sqrt{v^{2bottom} - v^{2top}}$. Including a regionally constant anisotropy at the top of the refractor, $\delta v_m^{anis}(\theta)$, and an azimuthal variation of the velocity gradient with depth, $\delta v_m^{grad}(\theta)$, in the model, and replacing $\delta v_m(\theta)$ in eqs (4) and (6) by $\delta v_m^{anis}(\theta) + \delta v_m^{grad}(\theta)$, then the traveltime, t_k, for a laterally homogeneous medium (number of blocks equals 1 and thus $\delta v_m^{(l)} = 0$) is

$$t_k = a_i + a_j + \frac{D_{ij}}{v_m} + \frac{1}{v_m^2}(F_i + F_j - D_{ij})[\delta v_m^{anis}(\theta) + \delta v_m^{grad}(\theta)], \quad (11)$$

where $\delta v_m^{anis}(\theta) = A \sin 2\theta + B \cos 2\theta$. In the above equation, the quantities F_i, F_j, v_m, A and B have to be assumed to be known at the start of an iteration. Thus the above equation is solved iteratively by least squares until no significant change (100 m in the case of F_i and F_j, 0.001 km s^{-1} in the case of v_m, and 0.01 km s^{-1} in the case of A and B) in these quantities occurs from one iteration to the next. In this study F_i and F_j were initially set to 30 km, while $\delta v_m^{grad}(\theta)$, for the calculation of which knowledge of A, B and v_m is required, was initially set to zero. For the data sets considered here, four iterations were usually necessary to obtain convergence.

Another model that we have used to test the P_n traveltime data is one in which the refractor velocity can be considered as a function of distance only (Smith, Steinhart & Aldrich 1966). In this approach the refracting layer is considered to be isotropic and laterally homogeneous, and $v = v_m^{top} + \varepsilon D_{ij}$, where ε is a constant expressing the velocity dependence on distance (Table 1). It can be noted that this relationship results in a monotonically decreasing velocity gradient with increasing depth, and not in a constant velocity gradient with depth.

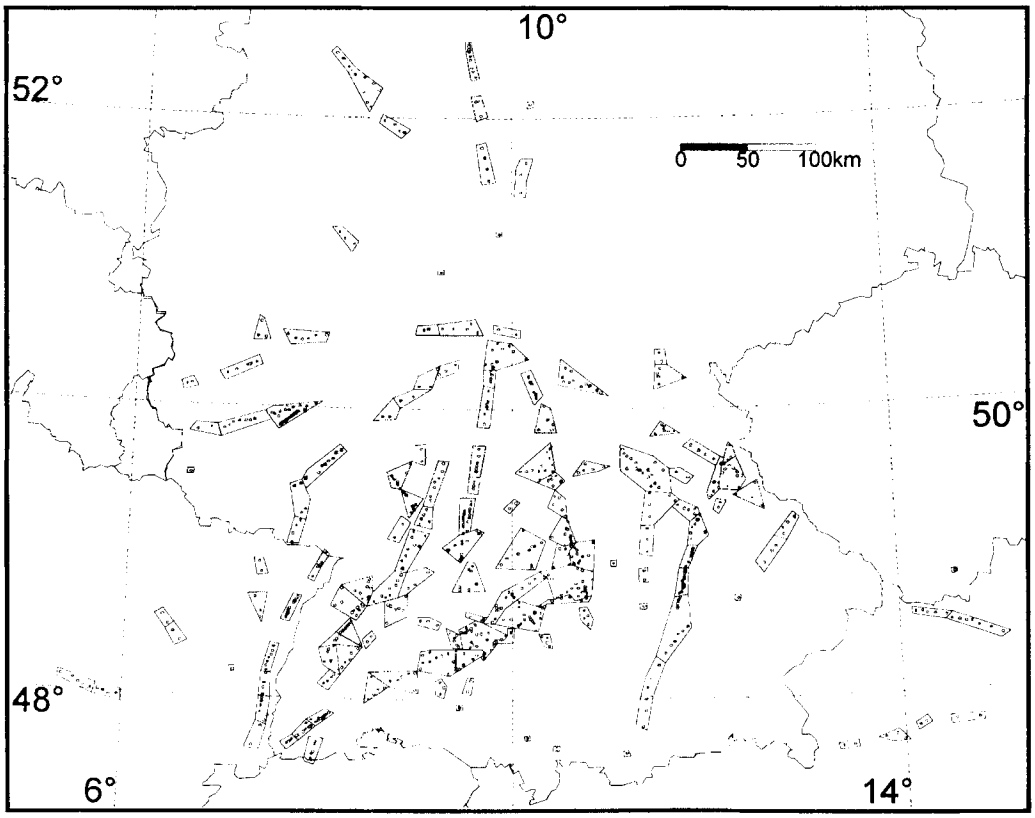

Figure 4. Areal distribution of shotpoints and sites where P_n has been recorded. Polygons surrounding selected sites are the so-called mosaics and are assumed to correspond to a single time term. The limits of the mosaics are based on geology.

3 P_n DATA AND RESULTS OF TRAVELTIME INVERSION

3.1 Seismic data from southern Germany

The network of seismic profiles in south-west Germany (Fig. 2) used in this study includes the original 639 P_n data of Bamford (1973), 123 data from the Rhinegraben experiment of 1972 (Edel *et al.* 1975), also used by Bamford (1976b, 1977), and the new data. The new data comprise 120 first arrivals from the Urach experiment of 1978–79 (Gajewski & Prodehl 1985), the Wildflecken experiment of 1982 (Zeis, Gajewski & Prodehl 1990), the Schwarzer Zollernwald experiment of 1984 (Gajewski & Prodehl 1987) and the European Geotraverse experiment of 1986 (EUGEMI Working Group 1990), thus a total of 882 data were available for this study.

Two record section examples from profiles that cross at an angle of about 55° are presented, one (Profile 01-315) from the original data of Bamford (1973), the other (Profile Z1-010-WF) from the Schwarzer Zollernwald experiment of 1984 (Fig. 3). In addition to the traveltime correlation shown here as a least-squares straight-line fit, examples of the peak-to-peak amplitudes of the P_n phase and the dominant crustal phase are also marked. From the linear regression for the profile Z1-010-WF, with P_n amplitudes of high energy, an apparent velocity of about 8.4 km s^{-1} is obtained, while for the profile 01-315, where the P_n phase is hardly visible, an apparent velocity of about 7.95 km s^{-1} is obtained. At this stage, the apparent velocities are not very predictable, but they indicate an azimuth-dependent tendency of P_n traveltimes and amplitudes, as discussed by Fuchs (1983).

The distribution of individual shots and stations where arrivals were recorded is shown, together with the distribution of the mosaics (Fig. 4). The mosaics are small areas beneath which the lateral and azimuthal variation of crustal delay times is considered to be negligible. The size of the mosaics ranges from single sites to a maximum side length of 50 km in a few cases. However, the majority of mosaics have side lengths less than 30 km, which is approximately the offset distance F_i (see Fig. 1) for P_n observations. Here, the mosaics are based on geology, and those from Bamford (1976a) are included. For the purpose of adding the necessary new mosaics, the Geological Map of the Federal Republic of Germany (1973) at a scale of 1 : 1 000 000 was referred to. This was sufficient to allow the definition of the mosaics so that, for example, tectonic boundaries such as faults could be avoided. Bamford (1976a, 1977) also designed mosaics based on Bouguer gravity and found that the solutions based on these mosaics were similar to the geology-based mosaics. Thus in this study only geology-based mosaics were analysed.

3.2 Results of time-term analysis for the uppermost mantle

3.2.1 Laterally homogeneous mantle

In this study, the P_n traveltime picks of Bamford (1973, 1976b) have been adopted. This facilitates comparison between the

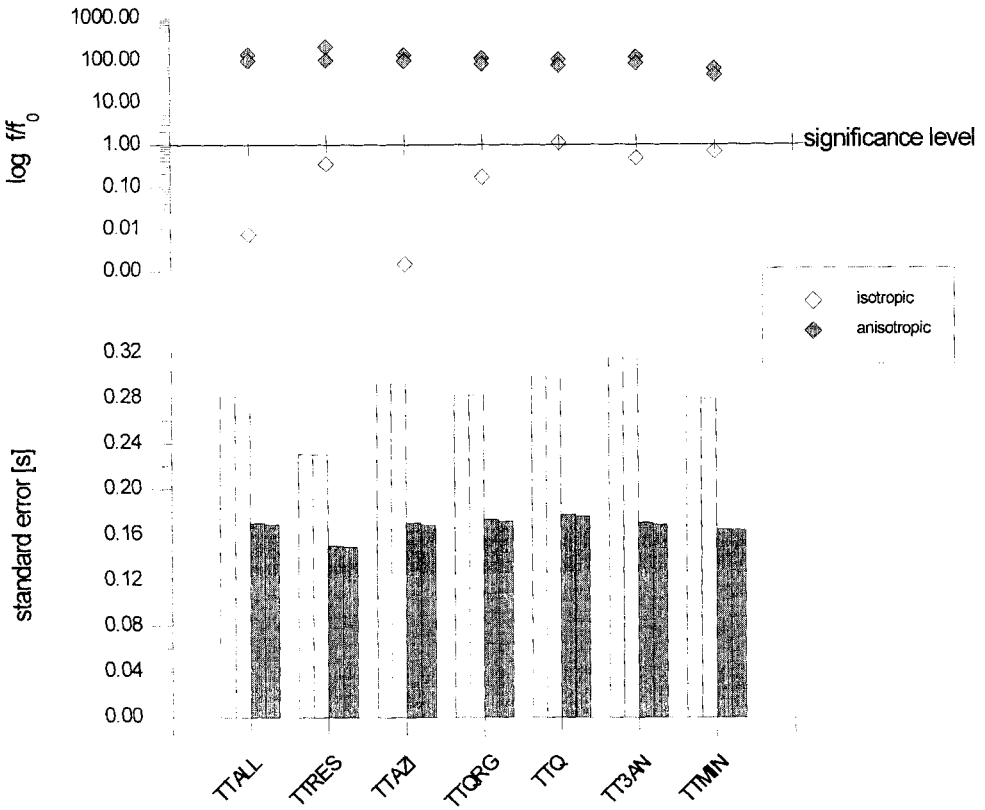

Figure 5. Standard errors and F-values for various time-term solutions. Note that all anisotropic solutions show a significant improvement in the traveltime fit. The solution with a constant refractor velocity was taken as the reference for the F-test. The y-axis in the upper diagram is displayed on a logarithmic scale in order to compress the range of F-values.

Table 1. Summary of the results of seven representative inversions for a laterally homogeneous medium. For each data set four assumptions for the refractor velocity v are made: (1) $v = v_m$; (2) $v = v_m^{top} + \varepsilon D_{ij}$; (3) $v = v_m + A\sin(2\theta) + B\cos(2\theta) + C\cos(4\theta) + D\sin(4\theta)$; (4) $v = v_m + A\sin(2\theta) + B\cos(2\theta)$. In addition to the time-term parameters v_m, A, B, C, D, ε (see Section 2.1), the standard error δ and the F value (eq. 12) are shown for each solution.

dataset name	p_n-data [no.]	MOZAICs [no.]	standard error δ [s]	v_m [km/s]	A [km/s]	B [km/s]	C [km/s]	D [km/s]	ε [0.001/s]	F-test
TTALL	882	139	0.28115	8.17±0.03	-	-	-	-	-	(reference)
			0.28133	8.21±0.19	-	-	-	-	-0.10±0.06	0.05
			0.16912	8.07±0.02	0.223±0.009	0.150±0.014	-0.018±0.010	0.045±0.013	-	328.16
			0.17037	8.07±0.02	0.233±0.009	0.167±0.013	-	-	-	640.33
TTRES	869	139	0.23051	8.18±0.02	-	-	-	-	-	(reference)
	869		0.23030	8.44±0.18	-	-	-	-	0.00±0.00	2.33
	870		0.14950	8.08±0.02	0.221±0.009	0.150±0.013	-0.024±0.009	0.037±0.012	-	355.70
	872		0.15053	8.10±0.02	0.250±0.009	0.147±0.012	-	-	-	979.47
TTAZI	771	130	0.29242	8.16±0.03	-	-	-	-	-	(reference)
			0.29265	8.18±0.21	-	-	-	-	-0.07±0.65	0.01
			0.16880	8.06±0.02	0.243±0.010	0.153±0.015	-0.004±0.010	0.055±0.010	-	321.16
			0.17050	8.06±0.02	0.257±0.010	0.174±0.015	-	-	-	622.27
TTQRG	762	128	0.28286	8.16±0.03	-	-	-	-	-	(reference)
			0.28283	8.38±0.22	-	-	-	-	-0.73±0.69	1.13
			0.17182	8.07±0.02	0.214±0.010	0.163±0.016	-0.012±0.010	0.058±0.016	-	271.63
			0.17370	8.07±0.02	0.229±0.010	0.188±0.016	-	-	-	523.80
TTQ	639	110	0.29924	8.17±0.03	-	-	-	-	-	(reference)
			0.29741	8.99±0.03	-	-	-	-	-2.74±1.02	7.52
			0.17636	8.05±0.03	0.203±0.011	0.188±0.023	-0.007±0.012	0.054±0.016	-	249.03
			0.17790	8.03±0.02	0.212±0.011	0.226±0.020	-	-	-	483.95
TT3AN	539	83	0.31501	8.21±0.03	-	-	-	-	-	(reference)
			0.31426	8.75±0.33	-	-	-	-	-0.20±0.10	3.17
			0.16936	8.05±0.03	0.238±0.013	0.204±0.025	-0.049±0.019	-0.006±0.022	-	280.78
			0.17071	8.11±0.03	0.243±0.012	0.176±0.019	-	-	-	548.16
TTMIN	374	68	0.28079	8.36±0.05	-	-	-	-	-	(reference)
			0.27917	9.33±0.28	-	-	-	-	-3.51±1.69	4.55
			0.16427	8.03±0.05	0.219±0.018	0.282±0.039	-0.066±0.033	0.025±0.032	-	147.54
			0.16508	8.10±0.04	0.221±0.017	0.287±0.030	-	-	-	289.71

solutions obtained in this study and those obtained by Bamford. Table 1 shows a summary of the results of five representative inversions for a laterally homogeneous medium including the new data and, for comparison with the results of Bamford (1976a, 1977), two inversions excluding the new data. For each data set the calculated least-squares values and the standard error, δ (see Bamford 1973, eq. 11), which is a measure of how well the velocity model fits the traveltime data, of each solution are shown.

The solution TTALL includes all available P_n data. To reject possible mispickings of P_n onsets, the solution TTRES involves the removal of those data whose traveltime residual is greater than three times the standard deviation of the solution TTALL. The solution TTAZI involves the removal of three profiles (01-020-09, Z1-010-WF, HS-190-Z1) in the azimuthal range N 0–20° in order to provide a more even distribution of observations with respect to azimuth. The results (Table 1) show that the effect on the solution of the removal of these three profiles, as well as the effect of the removal of two further profiles (01-005, SB-010-WI) to produce a fictitious minimum in the azimuthal range N 0–20°E, is minimal. Thus the azimuthal orientation of the fast axis of velocity in the N15–30°E azimuthal range is unlikely to be related to the fact that many observations occur in the azimuthal range N 0–20°E.

A comparison of the solutions TTQRG, which contains the original 639 P_n data plus the 123 Rhinegraben P_n data, and TTQ, which contains only the original 639 P_n data, with the solutions C^* and D^* of Bamford (1977), shows only minor differences, and thus it can be concluded that the iterative correction for the offset distance applied in this study causes no significant change in the results. Finally, the solutions TT3AN, which includes only observations in the south-west German triangle, and TTMIN, which includes only observations from the western part of the south-west German triangle, represent the smallest data sets that were analysed. These small data sets show more or less the same features as the larger ones.

Fig. 5 shows clearly the reduction in the standard error of each solution by about 35–45 per cent when anisotropy is allowed to be present. In this study the statistical F test is also used to examine the significance of an individual time-term solution compared to a reference. Taking the solution for constant refractor velocity as the reference, an F-test value for each modified solution can be computed with the following formula (Zervas & Crosson 1986):

$$f = \frac{\delta_u^2 N_u - \delta_m^2 N}{\delta_m^2 [N_u - N_m]}, \tag{12}$$

where δ is the standard deviation of the time-term solution and N is the degree of freedom of the system of equations. The index u stands for the reference solution, while the index m stands for the modified solution. The computed F-test values can be compared with theoretical F values (f_0) taken from tables for a confidence level of 99 per cent. For each solution that is considered to be a significant improvement, the ratio f/f_0 should be greater than 1. As the F test shows (Fig. 5), only the anisotropic solutions are clearly above the significance level and are therefore significantly better than the solution

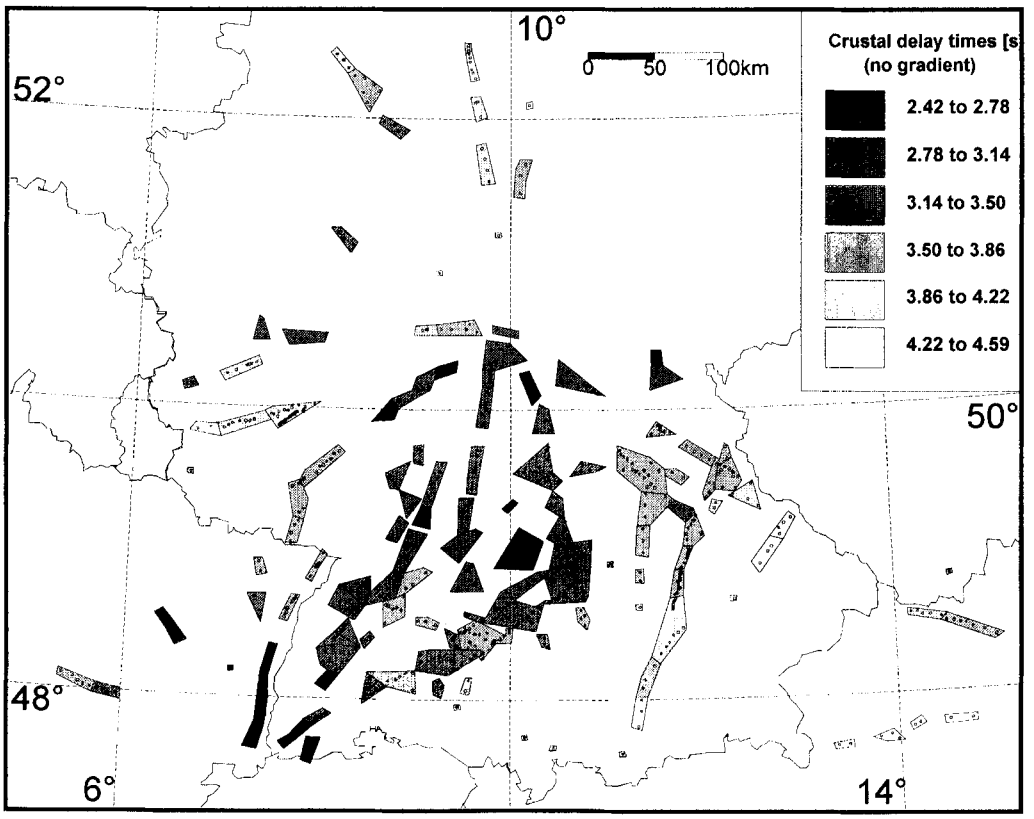

Figure 6. Crustal time terms (delay times) obtained by time-term solutions without sub-Moho gradients. Moho depths can be obtained by multiplying the delay times by 8.97 assuming an average crustal velocity of 6 km s^{-1}. Note that the smallest delay times occur in a SW–NE trending region, including the Rhinegraben. They increase towards the SE (Alps) and NW (Rhenish Massif).

with a uniform velocity. The solutions for the 2θ and 4θ anisotropy are practically indistinguishable from the statistical point of view. Due to the much higher errors of the 4θ terms compared to the 2θ terms (Table 1), the 2θ solution is taken to be more reliable. When anisotropy is allowed in the solutions the mean refractor velocity decreases from 8.15–8.2 km s^{-1} to 8.05–8.1 km s^{-1}, the magnitude of the anisotropy is 0.55–0.60 km s^{-1} and the direction of the maximum velocity is N 15–30°E.

In this study an average crustal velocity of 6.0 km s^{-1} has been used in calculating the values of F_i and $F_i\delta v^l$ for the next iteration. Calculation of the average crustal velocities from the velocity–depth functions for a variety of profiles in south-west Germany (Zeis *et al.* 1990) shows that the values range from 5.8–6.2 km s^{-1} and thus it is felt that 6.0 km s^{-1} is a reasonable value. For the data set TTALL and the solution involving anisotropy with 2θ terms only, the choice of 6.0 km s^{-1} for the average crustal velocity resulted in a mean refractor velocity of 8.07 km s^{-1} and a magnitude for the anisotropy of 0.57 km s^{-1}. Using an average crustal velocity of 5.8 km s^{-1} resulted in a mean refractor velocity of 8.06 km s^{-1} and a magnitude for the anisotropy of 0.54 km s^{-1}, while using an average velocity of 6.2 km s^{-1} resulted in a mean refractor velocity of 8.07 km s^{-1} and a magnitude for the anisotropy of 0.62 km s^{-1}.

For the data set TTRES, a map of crustal time terms (delay times) is shown (Fig. 6). In general the delay times reflect Moho topography as well as laterally varying velocity in the crust. Using an average crustal velocity of 6.0 km s^{-1}, Moho depths can be obtained by multiplying the delay times by 8.97. An average crustal velocity of 5.8 km s^{-1} would have caused a decrease in Moho depths of around 7 per cent while an average crustal velocity of 6.2 km s^{-1} would have caused an increase in Moho depths of about 8 per cent. The smallest Moho depths/delay times occur in a SW–NE trending region, including the Rhinegraben. Moho depths/delay times increase towards the SE (Alps) and NW (Rhenish Massif). This is in good agreement with a map of Moho depth isolines compiled by Zeis *et al.* (1990), which is based on single-profile interpretation.

3.2.2 *Horizontal velocity variations*

To study horizontal velocity variations of the uppermost mantle the refractor has been divided into blocks (Fig. 1). The number of blocks can be increased until the solution of the

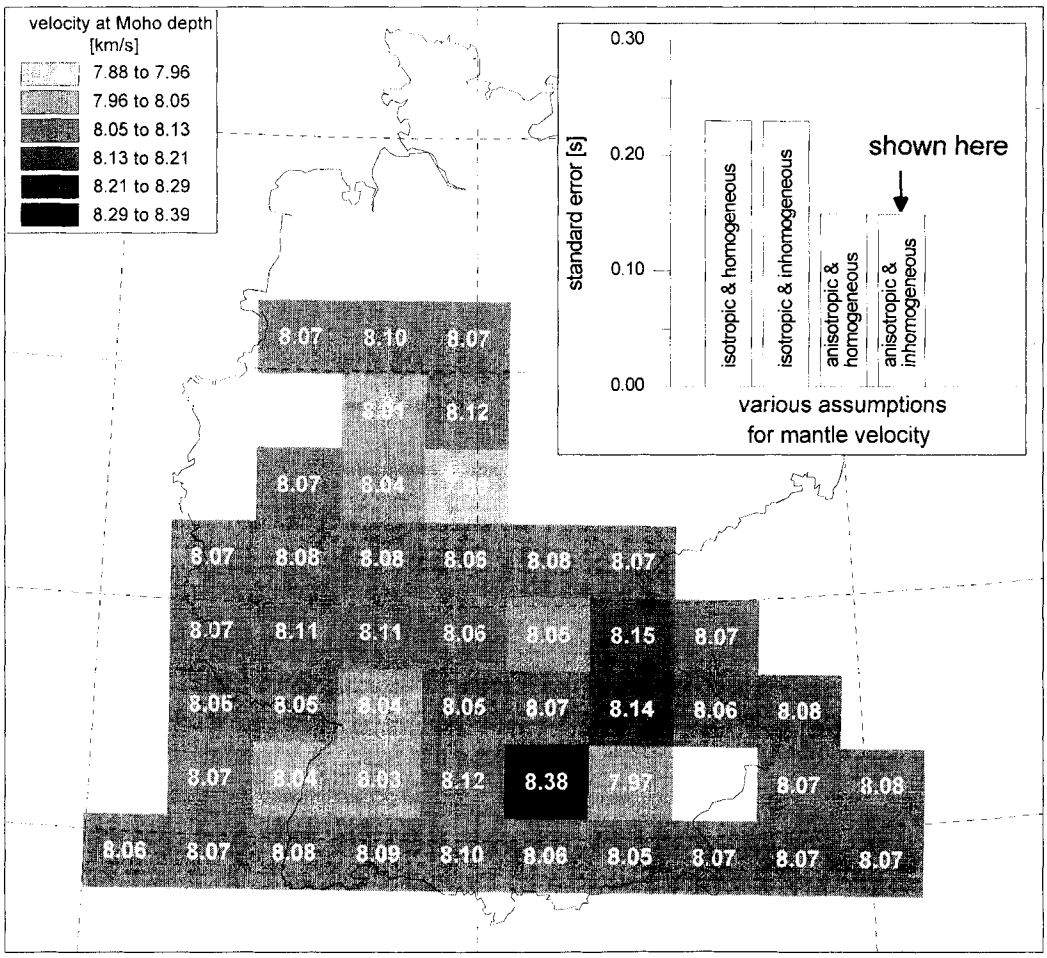

Figure 7. Laterally inhomogeneous model superimposed with a regional anisotropy. Except for five of the 47 blocks shown, the lateral mean velocity variation lies in a range of ± 0.06 km s^{-1}. Note that the standard error of this solution has not improved in comparison to the anisotropic and homogeneous solutions (inset). The diagram (inset) shows clearly that the reduction of the standard error is due to anisotropy.

traveltime inversion becomes unstable and has to be damped. Fig. 7 shows a block model for 100 blocks. The large number of blocks means that some blocks contain much less data than others and thus the individual block velocities can show considerable fluctuation. In this case, only the 47 blocks that contain enough data for them to be resolved at a satisfactory level are shown. Eq. (6) is solved by the method of damped least squares suggested by Hearn (1984):

$$(\mathbf{P}^T\mathbf{P} + c\Delta)\mathbf{x} = \mathbf{P}^T\mathbf{T} + c\Delta\mathbf{b}_0, \quad (13)$$

where $\mathbf{P}$ is the matrix of observation coefficients (Berry & West 1966), $\mathbf{T}$ is the observed traveltimes (data) vector, Δ is a diagonal matrix that is 1 if the unknown parameter is to be damped and 0 if it is not to be damped, $\mathbf{b}_0$ is a vector consisting of zeros or the velocity values to which the solution is to be damped, and c is the damping factor. To obtain a reasonable solution, *a priori* damping factors of about 20 000–30 000 were used.

The block-model solutions, which include lateral refractor velocity variations in addition to a regional anisotropy, show little improvement in the standard deviation with respect to the homogeneous solutions including anisotropy only. Considering only lateral variations provides a much poorer fit than including anisotropy (see inset of Fig. 7). Additionally, almost 80 per cent (36 out of 47) of the blocks in Fig. 7 have more or less the same mean velocity of 8.05–8.13 km s^{-1}. Also, the F-test values show that the block-model solutions are not much more significant than the solutions including anisotropy only. Thus it can be concluded that lateral velocity variations are not as important as anisotropy in south-west Germany.

So far, only traveltime information has been used in the inversion process. However, important information about a sub-Moho gradient can be obtained by analysing the amplitude behaviour of the P_n phase, and this can then be included in the inversion process of the traveltimes.

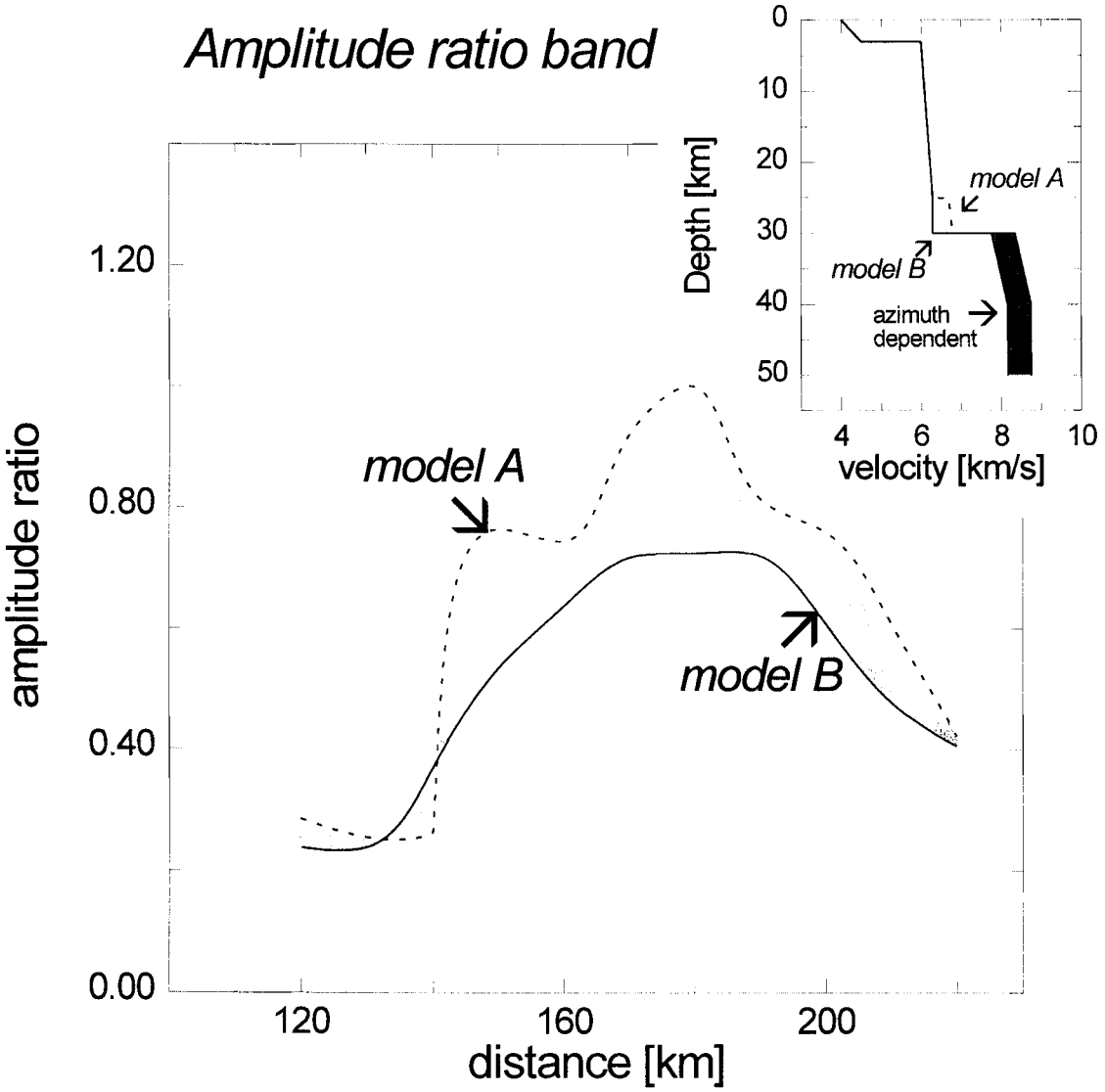

Figure 8. Two extreme crustal models (inset) and the resulting amplitude ratio band for a sub-Moho gradient of 0.04 s^{-1}. Model B has a very low lower-crustal velocity and thus a larger velocity contrast at the Moho and model A has a high lower-crustal velocity and thus a smaller velocity contrast at the Moho. Synthetic amplitude ratio–distance curves obtained with the anisotropic reflectivity method for both crustal models are taken as bounds for the amplitude ratio band.

4 ANALYSES OF P_n AMPLITUDES (BAND METHOD)

In order to continue the time-term model to greater depth, the azimuthally dependent velocity gradient in the uppermost mantle (sub-Moho) layer had to be determined. As amplitudes are more sensitive to gradients than traveltimes, this was accomplished by quantitatively analysing amplitudes from 12 azimuthally distributed profiles in a 250 × 300 km area in the western part of the southern Germany triangle (Fig. 2).

In the fast velocity direction, P_n amplitudes that are large compared to the amplitudes of the dominant crustal phase(s) can often be observed (Bamford 1977; Fuchs 1983). The ratios of the P_n amplitudes to the amplitudes of the dominant crustal phase were compared with theoretical amplitude ratios for different velocity gradients in the uppermost mantle layer.

The theoretical amplitudes were calculated using the reflectivity method for anisotropic media (Booth & Crampin 1983; Nolte 1988). The computer code used in this study only includes integration over the horizontal slowness in the sagittal plane (the vertical plane through the shot and the station). The horizontal slowness at right angles to the sagittal plane is equal to zero. Nolte, Frazer & Mallik (1992) have made calculations with integration over both horizontal slownesses and have estimated that neglecting the horizontal slowness at right angles to the sagittal plane still produces sufficiently precise results for traveltimes and amplitudes in most cases of weak anisotropy, even when wave propagation occurs significantly outside the sagittal plane.

To take into account the effects of the crustal structure, two extreme crustal models were utilized (Fig. 8). One of these models (B) has a very low lower-crustal velocity of 6.3 km s^{-1} and thus a larger velocity contrast at the Moho. The dominant crustal phase in this model over the distance range of interest is the Moho reflection (P_MP). The other model (A) has a high lower-crustal velocity of 6.7–6.8 km s^{-1} and thus a smaller velocity contrast at the Moho (Zeis *et al.* 1990). In model A the dominant crustal phase over the distance range of interest is either P_MP or the reflection from the top of the 6.7–6.8 km s^{-1} basal crustal layer. The use of two extreme crustal models counteracts the trade-off between the Moho velocity jump and the velocity gradient in the uppermost mantle layer. The velocity immediately below the Moho in the

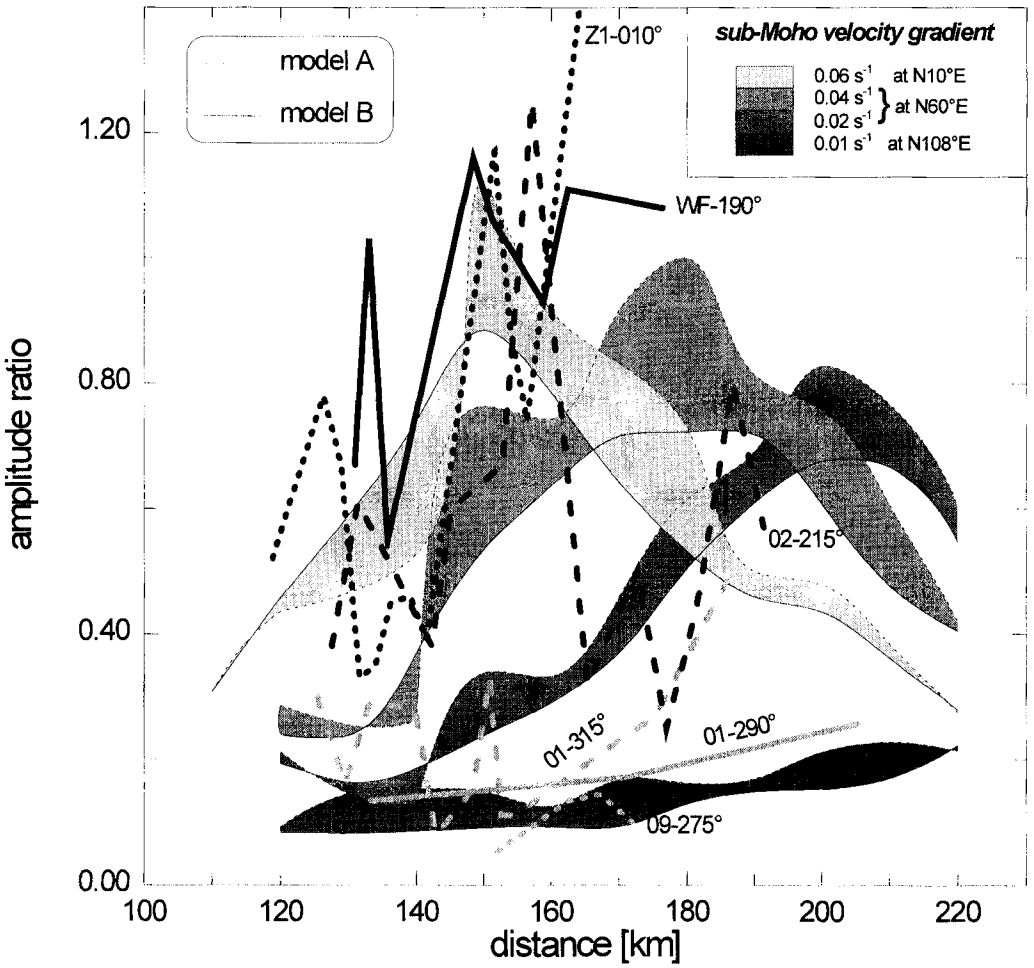

Figure 9. Amplitude ratio bands for the time-term solution uncorrected for the sub-Moho velocity (anisotropy) gradient. Each 'band' represents a range of amplitude variation with distance for one fixed sub-Moho gradient. Different sub-Moho gradients are indicated by different bands with different grey values. The observed amplitude ratio data from six profiles are shown as thick lines with a different line style for each profile. Profiles from the direction of higher P_n velocities are drawn in black and profiles from the direction of lower P_n velocities are drawn in grey.

fast anisotropy direction is 8.4 km s^{-1}, whilst in the slow velocity direction it is 7.8 km s^{-1}. For reasons given below (Section 7), the uppermost mantle layer has been taken to be 10 km thick and to overlie a half-space.

As an example, amplitude ratios derived using the two extreme crustal models, A and B, are presented (Fig. 8) for a gradient in the uppermost mantle layer of 0.04 s^{-1} and a profile direction of N60°E, which is equivalent to 33° away from the fast velocity direction. Calculations using crustal models with velocities intermediate between these two extreme models show that the bands shown here can be taken as being reliable. Amplitude ratio curves (bands) for models A and B are shown in Fig. 9, in which amplitude bands for different velocity gradients are presented. In order to take into account the azimuthally dependent velocity jumps at the Moho, the amplitude ratio curves for the gradient 0.06 s^{-1} in the fast velocity direction are shown, as are the curves for the gradients 0.02 s^{-1} and 0.04 s^{-1} in the intermediate direction, and the curves for the gradient 0.01 s^{-1} in the slow velocity direction. The observed amplitude ratio data are shown in Fig. 9 as thick lines with different line styles for different profiles. These diagrams enable one to assign velocity gradients by eye to the corresponding profile azimuths. Despite the large fluctuations in the observed amplitude ratio curves and the fact that the synthetic amplitudes have been calculated only by integrating over the horizontal slowness in the sagittal plane, those curves from profiles in the fast velocity directions display high ratios and thus fit theoretical curves for large sub-Moho gradients, while those curves from profiles in the slow velocity direction display low ratios and thus fit theoretical curves for small sub-Moho gradients. This variation in velocity gradient with respect to azimuth is also an indication for anisotropy, as in an isotropic medium the velocity gradient at a particular place is independent of the direction of wave propagation.

From the comparison between the observed and theoretical amplitude ratio curves (Fig. 9), velocity gradients have been picked by eye for the 12 investigated profiles. These velocity gradients have been plotted against the profile azimuth (Fig. 10) and three curves have been fitted to this observed distribution. The first of these curves (NA-1) is for a sub-Moho gradient of 0.06 s^{-1} in the fast velocity direction and 0.01 s^{-1} in the slow direction, the second (NA-0) is for a gradient of 0.06 s^{-1} in the fast direction and 0 s^{-1} in the slow direction, and the third is a least-squares fit of the observed velocity gradient versus azimuth. Fig. 11 shows synthetic seismograms for the fast, intermediate and slow directions for the model NA-0 using crustal model A. Different amplitude variation with distance is obvious.

5 COMBINED P_n TRAVELTIME AND AMPLITUDE INVERSION

The results of the analysis of P_n amplitudes in the last section showed that strong gradients (0.06 s^{-1}) exist in the fast velocity direction and that weak gradients (0–0.01 s^{-1}) exist in the slow velocity direction. In the time-term analysis described in Section 3, no gradient in the upper mantle was taken into account, thus a further time-term analysis in which azimuthally dependent velocity gradients were taken into account using

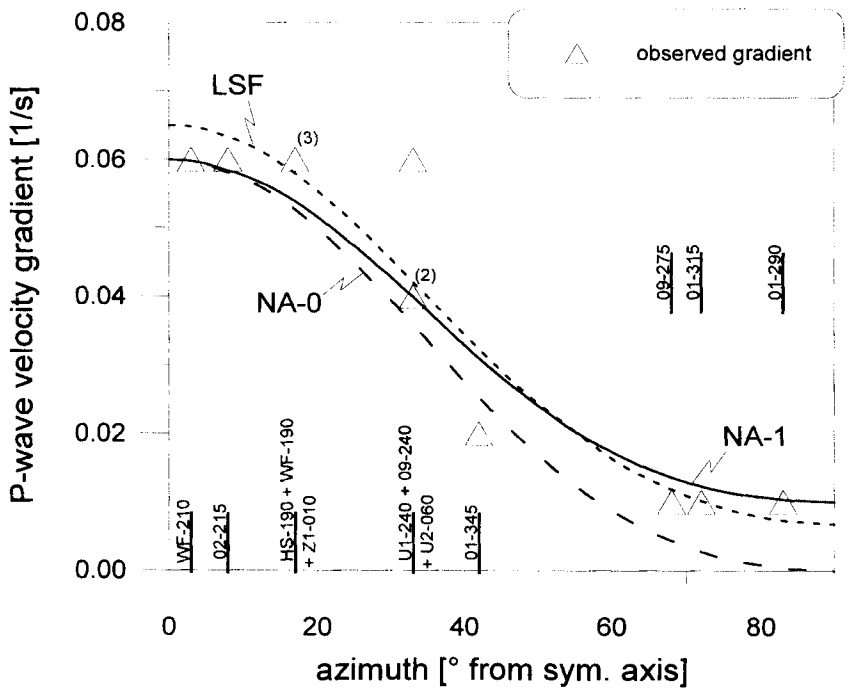

Figure 10. Velocity gradients obtained with the 'band method' are plotted versus the azimuth. The azimuth is measured in degrees from the symmetry axis and has been reduced to the first quadrant. The profile ID (Fig. 2) for each data point (Δ) is also shown. Multiple occurrence of data points is indicated by numbers. Three fits to the observed sub-Moho gradients are shown as lines with different styles. The first of these fits (NA-1) is for a sub-Moho gradient of 0.06 s^{-1} in the fast velocity direction and 0.01 s^{-1} in the slow direction, the second (NA-0) is for a gradient of 0.06 s^{-1} in the fast direction and 0 s^{-1} in the slow direction and the third (LSF) is a least-squares fit of the observed velocity gradient versus azimuth.

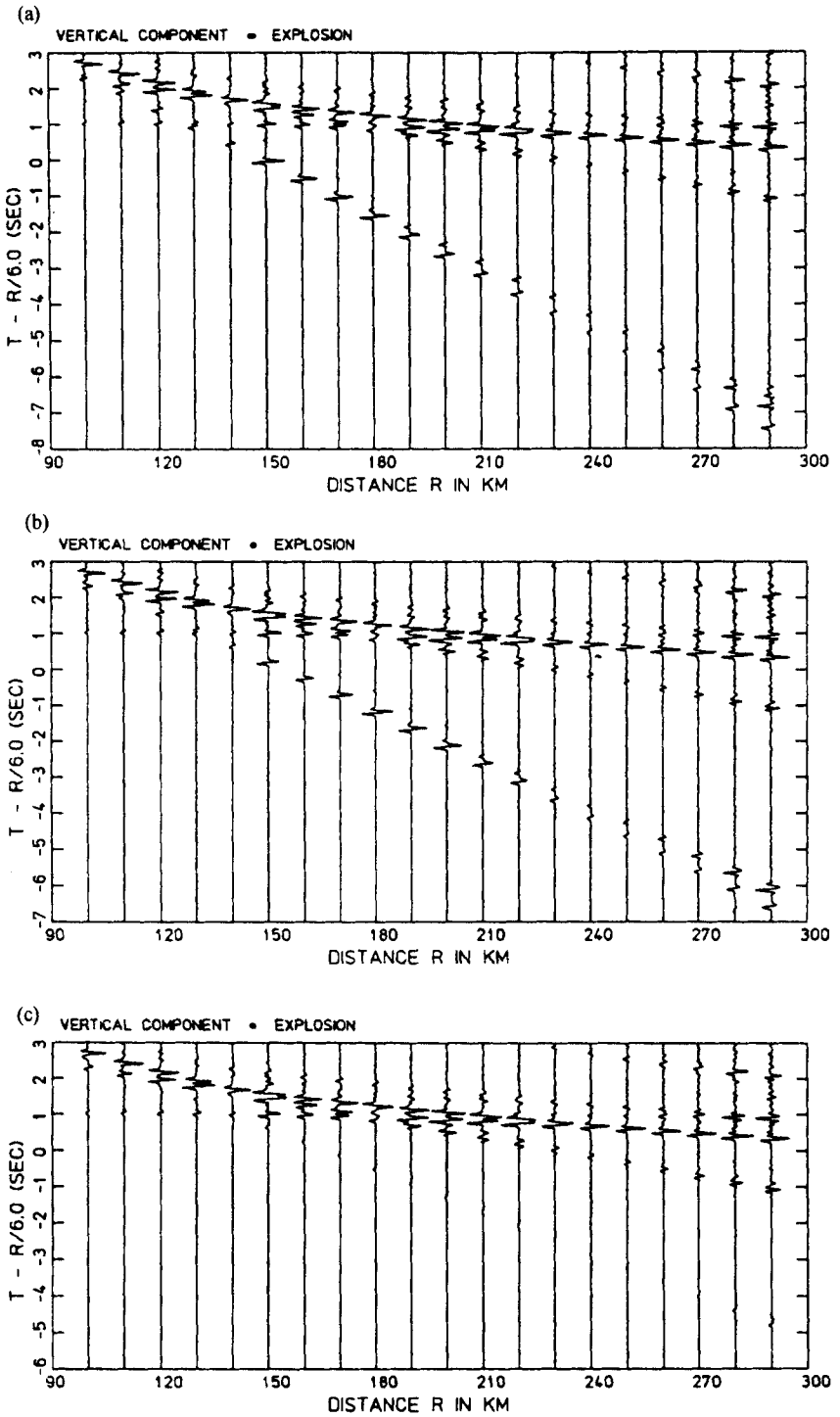

Figure 11. Synthetic seismograms for the fast (a), intermediate (b) and slow (c) directions for the model NA-0 using the crustal model A. Different amplitude variation with distance is obvious.

eq. (11) (see Section 2) was carried out. Various combinations of gradients in the fast and slow velocity directions were investigated. The gradient in the fast velocity direction was varied from $0\,s^{-1}$ to $0.06\,s^{-1}$, while the gradient in the slow velocity direction was held constant at $0\,s^{-1}$. The thickness of the layer with the gradient was also held constant at 10 km (the reasons for this are provided below in the summary and conclusions section), and below this layer a half-space with no gradient was assumed. The results indicate that the amount of anisotropy varies depending on the size of the gradient in the fast velocity direction. The anisotropy at the top of the layer, immediately beneath the Moho, is 3–4 per cent when the gradient is $0.06\,s^{-1}$ and increases to 6–7 per cent as the gradient decreases to $0\,s^{-1}$ (Fig. 12).

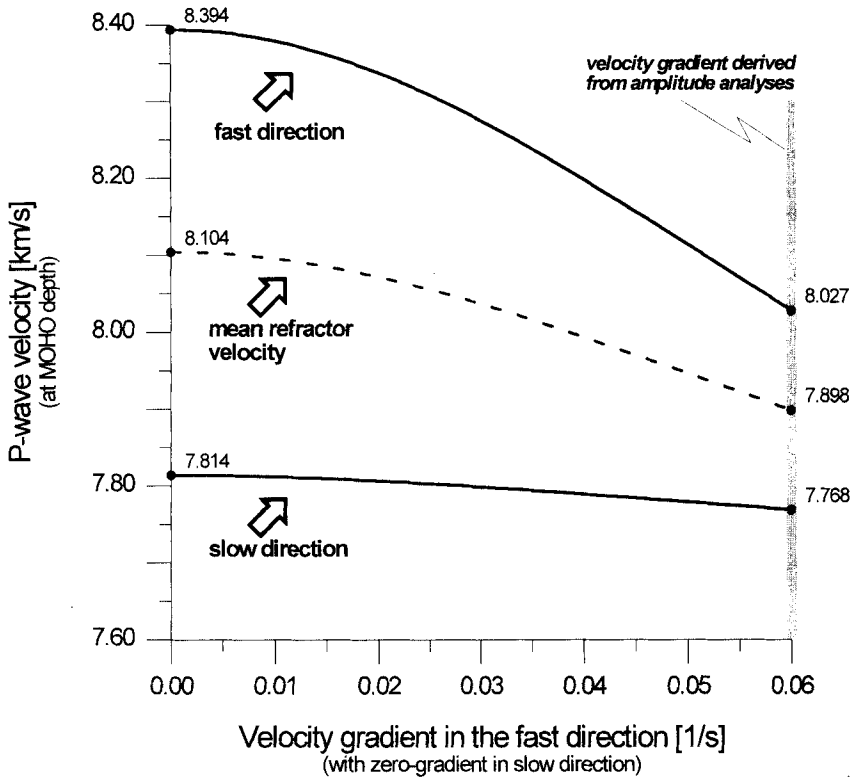

Figure 12. P_n velocities for various sub-Moho gradients obtained with the 'modified' time-term method. Note that the anisotropy decreases while the gradient in the fast direction increases. According to the results of the amplitude investigation the gradient in the slow velocity direction was held constant at 0 s^{-1} while the gradient in the fast velocity direction was increased to 0.06 s^{-1}. The new time-term solution, which includes the results of the amplitude analysis, is marked by a grey strip.

Theoretical seismograms were again calculated using the reflectivity method for anisotropic media (Booth & Crampin 1983; Nolte 1988) for the new model with 3–4 per cent anisotropy at the top of the 10 km thick layer and with a gradient of 0.06 s^{-1} in the fast velocity direction and 0 s^{-1} in the slow velocity direction. The two crustal models that were used in Section 4 were again used to produce amplitude ratio bands (Fig. 13). The amplitude ratios derived from the new model show approximately the same fit to the observed data as the amplitude ratios from the models in Section 4 and therefore confirm the azimuthal variation of sub-Moho velocity gradients shown in Fig. 10.

In order to fit the velocity gradient distribution resulting from the analysis of the P_n amplitudes, it would appear that the amount of anisotropy in the uppermost mantle beneath south-west Germany is around 3–4 per cent immediately below the Moho, increasing to about 11 per cent at about 10 km below the Moho. This is in reasonably good agreement with the previously derived average value of about 7 per cent (Bamford 1977). For the modified time-term analysis including the sub-Moho gradient, a new map of the crustal time terms (delay times) is shown (Fig. 14). In this map the pattern of the delay times remains unchanged in comparison to Fig. 6. The inset in Fig. 14 shows that the simultaneous inversion of traveltime and amplitude information results in an average increase of the crustal delay times of about 0.2 s. Assuming an average crustal velocity of 6 km s^{-1} this is equal to an average increase in Moho depth of about 1.8 km.

6 PETROLOGICAL MODELS

The petrological model is considered to be successful if it fits the following seismic, thermal and petrological (xenolith-derived) constraints.

6.1 Seismic constraints

As has been shown in the previous sections, the seismic observations require an anisotropic layer immediately below the Moho. In this anisotropic layer the seismic velocity for horizontally propagating waves should increase with depth, with high gradients of about 0.06 s^{-1} in the fast direction and low gradients of 0–0.01 s^{-1} in the slow direction. Taking into account possible errors, the following seismic velocity constraints are used:

$V_p = 8.03 \pm 0.05$ km s^{-1} at 30 km depth, fast direction;

$V_p = 8.63 \pm 0.05$ km s^{-1} at 40 km depth, fast direction;

$V_p = 7.77 \pm 0.05$ km s^{-1} at 30 km and 40 km depth, slow direction.

6.2 Thermal constraints

Surface heat-flow measurements in southern Germany (Blundell, Freeman & Müller 1992) show that the average surface heat flow is about 85 mW m^{-2}. Using this value, together with the Pollack & Chapman (1977) geotherms, results in temperatures of about 700 °C at the Moho at 30 km depth and about 850 °C

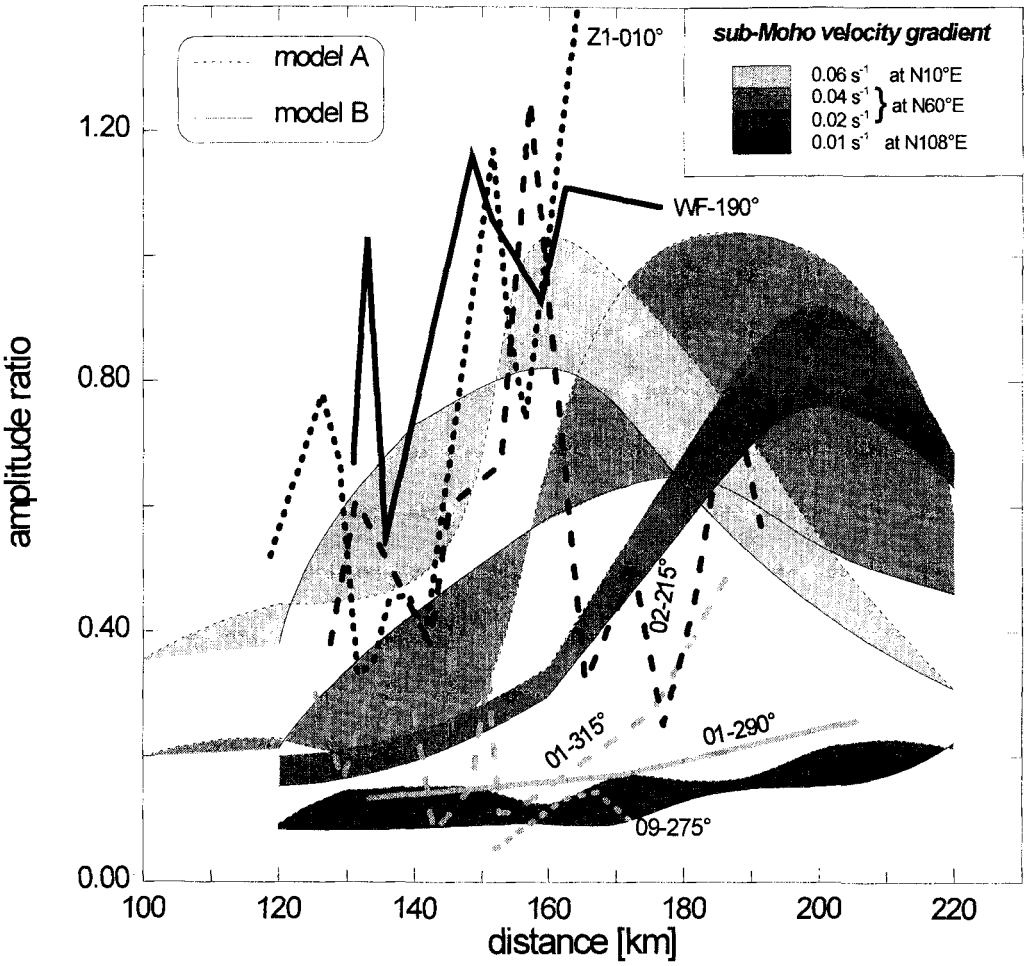

Figure 13. Recalculated amplitude ratio 'bands' for the modified time-term solution in which the sub-Moho velocity gradient has been taken into account. The gradient in the fast velocity direction is 0.06 s^{-1} and in the slow velocity direction it is 0 s^{-1}. Profiles from the fast velocity direction still correlate with high gradients and profiles from the slow velocity direction with low gradients. Assignment of gradients to the profile directions confirms the azimuthal variation of sub-Moho gradients shown in Fig. 10.

at 40 km depth. Taking into account possible errors, the following temperature constraints are used:

$T = 700 \pm 100\,°C$ at 30 km depth;

$T = 850 \pm 100\,°C$ at 40 km depth.

6.3 Xenolith constraints

Xenoliths are composed mainly of olivine-rich harzburgites in the Hegau, wehrlites in Urach and dunites in both localities (Sachs 1988). They contain 75–98 per cent olivine (Ol), with the average being about 80–85 per cent. A few samples of Ol-poor harzburgites (57–67 per cent Ol), spinel lherzolites (70 per cent Ol) and pyroxenites are also available (Fig. 15). We assume that the xenoliths represent the composition of the uppermost mantle in the area of seismic investigation.

The anisotropic elastic properties of the xenoliths can be calculated either from their observed bulk chemical composition (Sobolev & Babeyko 1994) or from their observed modal composition and the composition of the individual minerals. Olivine is assumed to be the only anisotropic phase. The seismic observations can be fitted by varying the fraction of preferentially oriented olivine grains and the *in situ* temperatures of the xenoliths. Under the assumption that flow direction in the continental upper mantle is almost horizontal, the *a*-axis will also be horizontal (Nicolas *et al.* 1971; Fuchs 1983). Therefore, possible models include *a*- and *b*-axes horizontal or *a*-axis horizontal and *b*- and *c*-axes as girdles. The latter class of models provides a much poorer fit (Fuchs 1983) and thus will not be further discussed. The *c*-axis cannot be horizontal as the observed maximum velocity is too large and the observed minimum velocity is too small.

The rock is considered to be a composite consisting of several minerals that can, in general, be anisotropic. In this study all minerals except olivine are assumed to be randomly and uniformly distributed, so the rock is considered to be a mixture of an isotropic part, which consists of all randomly and uniformly distributed mineral grains, and an anisotropic part, which consists of a number of populations of olivine grains with different orientations. The elastic tensor for the isotropic part is determined by two elastic moduli that are calculated as arithmetic means between the upper and lower Hashin and Shtrikman bounds (Hashin & Shtrikman 1962), respectively. The elastic moduli of minerals are taken from Duffy & Anderson (1989).

The elastic tensor for the rock is calculated using the

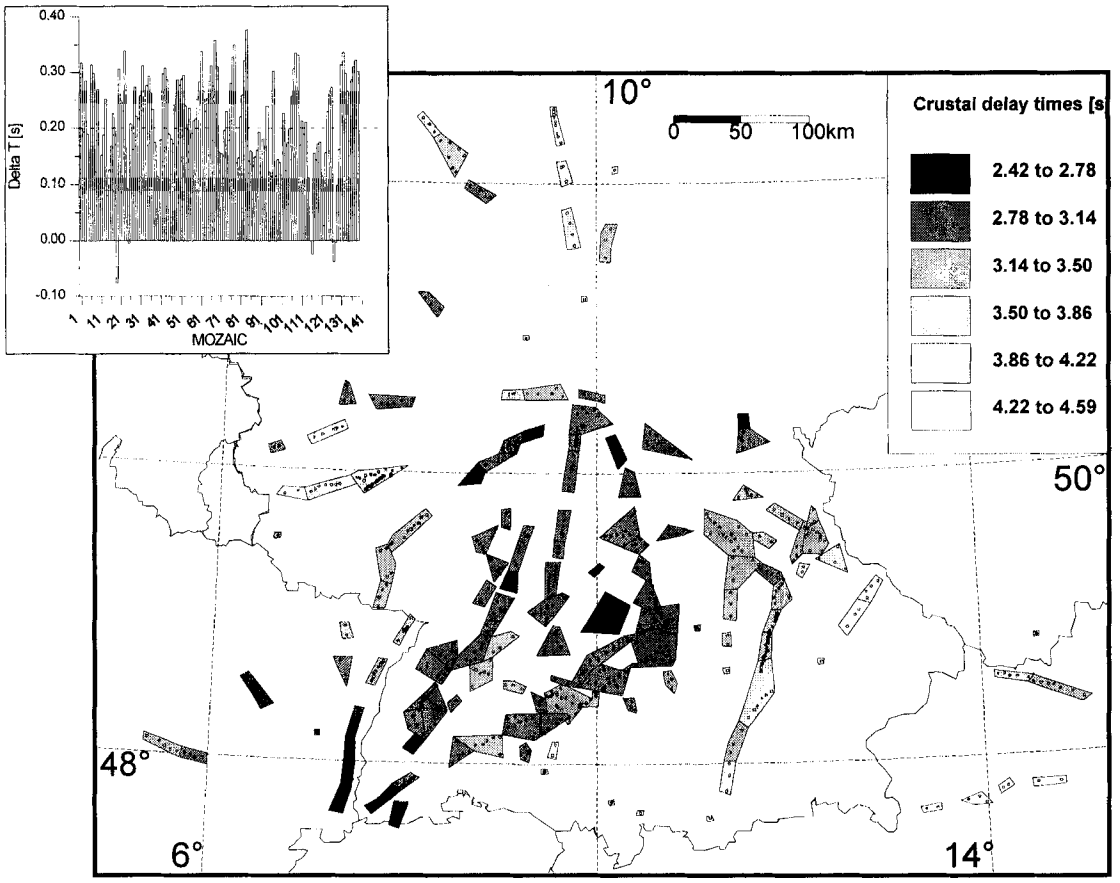

Figure 14. Crustal time terms (delay times) obtained by time-term solutions with a sub-Moho gradient of 0.06 s^{-1} in the fast and 0 s^{-1} in the slow velocity direction. Moho depths can be obtained by multiplying the delay times by 9.22 assuming an average crustal velocity of 6 km s^{-1}. The pattern of the delay times is more or less unchanged compared to Fig. 6. The inset shows the influence of the sub-Moho gradient on the crustal delay time of each mosaic. Note that there is an average increase of crustal delay times of about 0.2 s. Assuming an average crustal velocity of 6 km s^{-1} this is equal to an average increase in Moho depth of about 1.8 km.

following expression:

$$C_{ij}^{\mathrm{ef}} = (C_{ij} + S_{ij}^{-1})/2, \tag{14}$$

with

$$C_{ij} = V^{\mathrm{iso}} C_{ij}^{\mathrm{iso}} + \sum_l V_l C_{ij}^l,$$

$$S_{ij} = V^{\mathrm{iso}} S_{ij}^{\mathrm{iso}} + \sum_l V_l S_{ij}^l, \tag{15}$$

where C_{ij}^{ef} is the effective elastic stiffness tensor of the rock, C_{ij}^{iso} and S_{ij}^{iso} are the elastic stiffness and compliance tensors of the isotropic part of the rock (volume fraction V^{iso}) and C_{ij}^l and S_{ij}^l are the elastic stiffness and compliance tensors of the lth population of olivine grains with the volume fraction V_l. Although eq. (14) is not linear, it is preferred because in the isotropic limit it gives a better estimate of the effective elastic moduli (VRH average) than the linear expression (Voigt or Reuss average). The single-crystal elastic tensor of olivine and the partial derivatives with respect to temperature are taken from Isaak (1992) and the partial derivatives with respect to pressure are taken from Kumazawa & Anderson (1969).

For every xenolith sample we estimated the elastic tensor by scanning the fraction of preferentially oriented olivine grains and *in situ* temperature (within the imposed constraints) in order to fit the seismic observations. From this procedure we obtain the following model, which fits all of the above observations within the imposed constraints (plotted as Δ in Fig. 15; elasticity tensors are shown in Table 2). It consists of a 10 km thick layer of peridotites with their composition changing from Ol-poor harzburgite (57 per cent Ol) at the top to Ol-rich peridotite (90 per cent Ol) at the bottom. The fraction of preferentially oriented olivine grains varies from about 20 per cent at the top to about 40 per cent at the bottom. The temperature at about 30 km depth is about 700 °C. The azimuth-dependent *P*-wave velocity at a depth of 30 km for this model is shown in Fig. 16, together with a velocity scattergram (Zervas & Crosson 1986) and the best fit from the time-term analysis. This model is qualitatively similar to the previously suggested anvil model of Fuchs (1983), but implies a considerably higher composition–depth gradient (i.e. greater increase of Ol with depth), a lower fraction of preferentially oriented olivine and a higher Moho temperature. The differences between the models result mainly from the following:

(1) the updated values used for the seismic velocities in the fast direction (8.03 km s^{-1} at 30 km depth and 8.63 km s^{-1} at 40 km depth) are considerably lower than those used by Fuchs (1983) (8.35 km s^{-1} and greater than 9.0 km s^{-1});

(2) the velocity gradient in the slow direction is assumed to be either zero or low, but positive in contrast to the negative gradient suggested by Fuchs (1983);

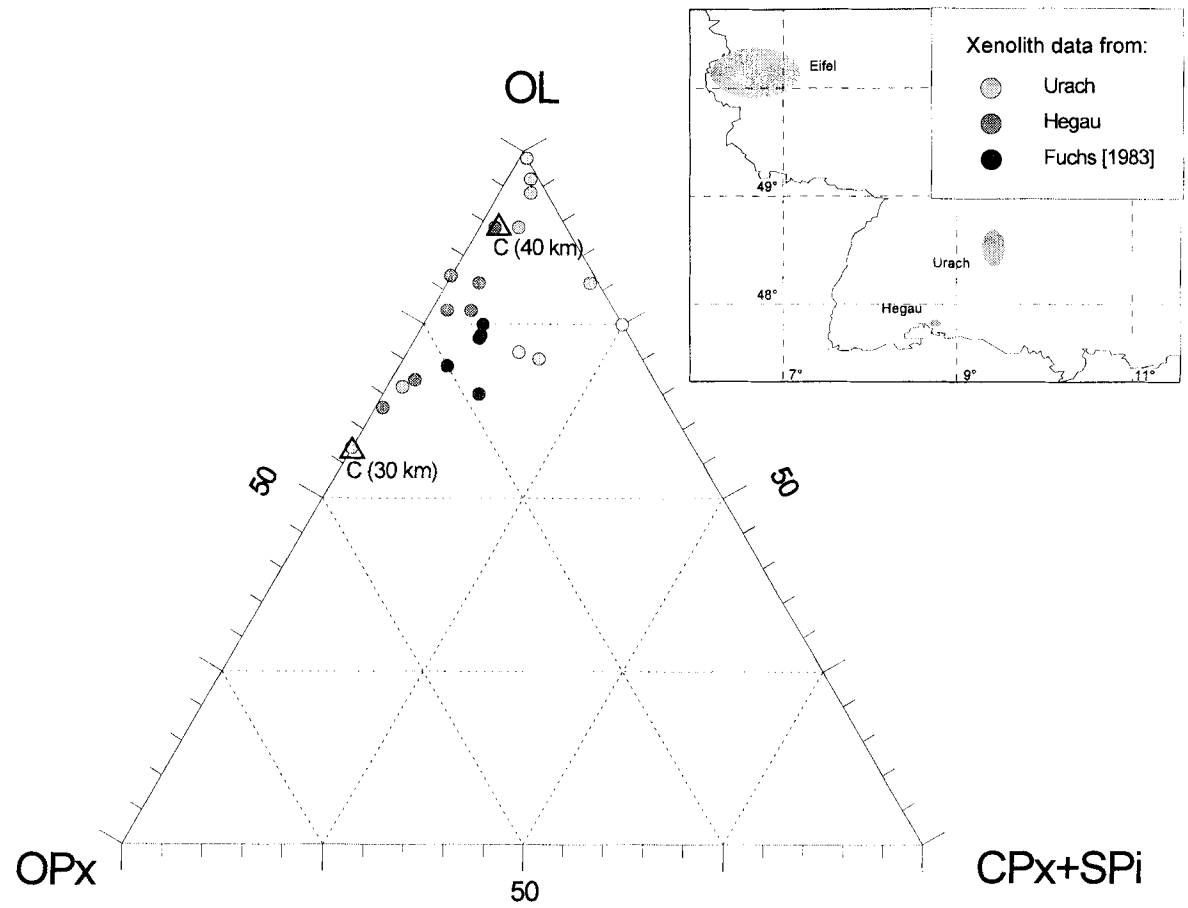

Figure 15. Mineral composition of xenoliths from southern Germany and petrological results (Δ). The modelled composition with 57 per cent OL fits the seismic, thermal and petrological constraints immediately below the Moho at 30 km depth, C (30 km), and the modelled composition with 90 per cent OL fits the same constraints at 40 km depth, C (40 km).

Table 2. Proposed elasticity tensors for the uppermost mantle beneath southern Germany at (a) 30 km depth (temperature $T = 690\,^{\circ}C$, pressure $P = 8.5$ kbar, density $\rho = 3.287$ g cm^{-3}, modal composition: 57.3 per cent OL, 42.7 per cent Opx) and (b) 40 km depth (temperature $T = 820\,^{\circ}C$, pressure $P = 11.8$ kbar, density $\rho = 3.291$ g cm^{-3}, modal composition: 89.5 per cent OL, 8.3 per cent Opx, 0.8 per cent Cpx, 1.4 per cent Spi). Elasticity constants c_{ijkl} are in GPa.

(a)

c_{ijkl}	(1,1)	(2,2)	(3,3)	(3,2)	(3,1)	(2,1)
(1,1)	211.88	63.90	64.72	-	-	-
(2,2)	63.90	198.47	65.45	-	-	-
(3,3)	64.72	65.45	203.33	-	-	-
(3,2)	-	-	-	67.00	-	-
(3,1)	-	-	-	-	68.64	-
(2,1)	-	-	-	-	-	68.64

(b)

c_{ijkl}	(1,1)	(2,2)	(3,3)	(3,2)	(3,1)	(2,1)
(1,1)	245.02	69.04	71.82	-	-	-
(2,2)	69.04	198.47	74.15	-	-	-
(3,3)	71.82	74.15	214.83	-	-	-
(3,2)	-	-	-	63.95	-	-
(3,1)	-	-	-	-	69.21	-
(2,1)	-	-	-	-	-	69.15

(3) the temperatures used here in the uppermost mantle are higher than those used by Fuchs (1983).

The model requires strong chemical inhomogeneity of the uppermost mantle. It is impossible to fit the seismic observations without a compositional gradient because it would require an increase in the fraction of preferentially oriented olivine grains above 100 per cent or a completely unrealistic geotherm (strong decrease of temperature with increasing depth). Although our model fits seismic and thermal observations as well as xenolith compositions, we admit that it is based on the very limited xenolith data that is available at present. For more reliable conclusions we need more data, including bulk chemical compositions of xenoliths, microprobe analyses of mineral compositions, and measurements of orientation of olivine and orthopyroxene grains in thin sections. We also note that the composition of the mantle predicted by our model immediately beneath the Moho is rather unusual. Low seismic velocities estimated at 30 km depth, together with temperature constraints, forced us to choose the composition of olivine-poor harzburgite (Ol 57 per cent), as this was the only composition from the reported peridotitic xenolith samples in southern Germany (Sachs 1988) that could fit the observations. Normally olivine-poor harzburgitic xenoliths are very rare, and it is likely that they result from interaction of peridotites with the mafic melt. Keeping this in mind, in a

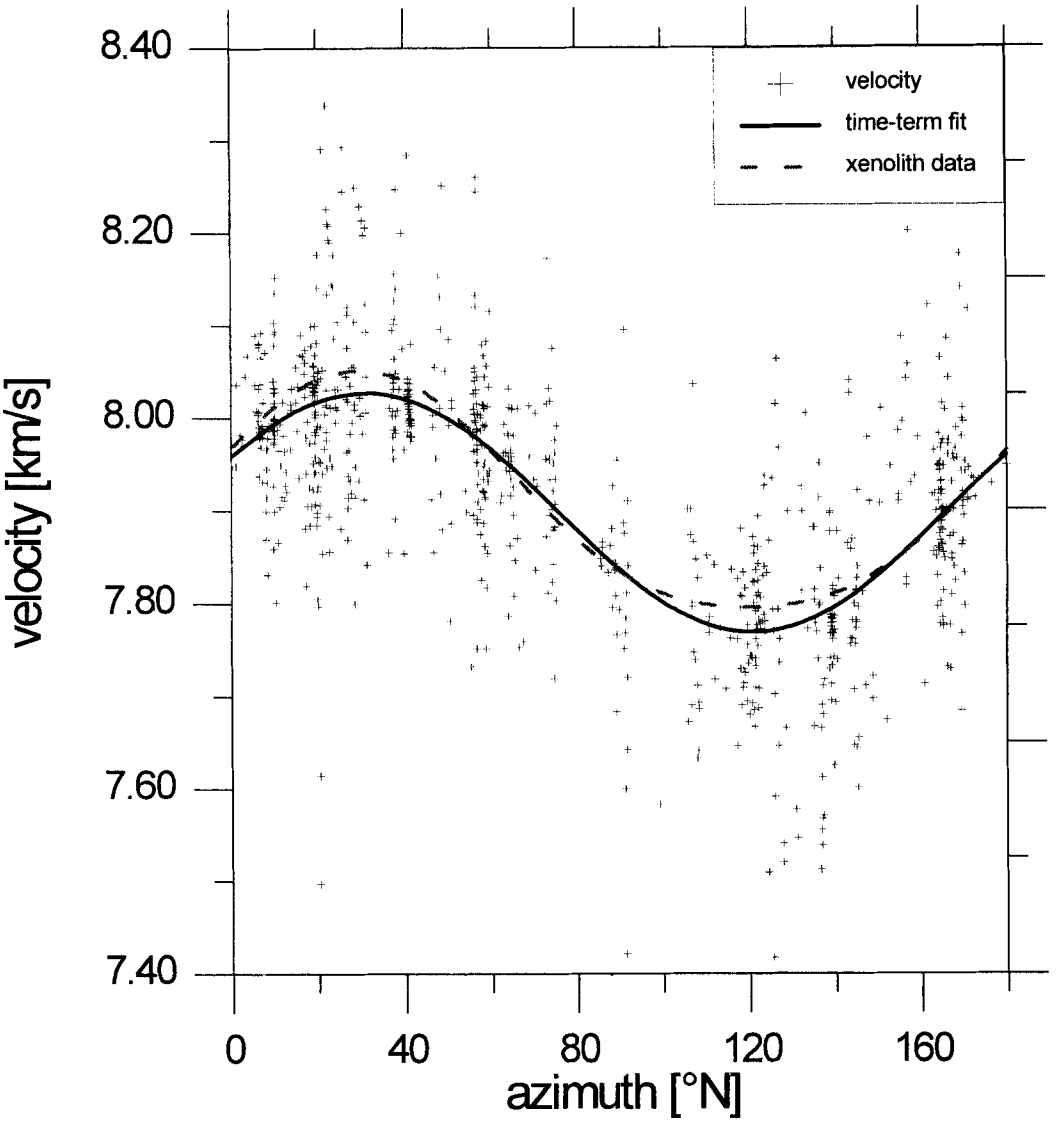

Figure 16. Velocity scattergram derived from the time-term solution with a gradient of 0.06 s^{-1} in the fast direction and 0 s^{-1} in the slow direction. Velocities are obtained by solving eq. (3) for δv_m, since the basic time-term parameters, a_i, a_j and v_m, are known from the time-term solution. The values of δv_m show that the data constrain the model variations significantly above the noise level. The best fit from the time-term solution (solid line) and the calculated velocities from the xenolith from southern Germany with the composition of 57.3 per cent OL and 42.7 per cent OPx (dashed line) are also shown. Note that the maximum deviation between these curves is less than 0.03 km s^{-1}.

further study we plan to investigate other possible petrological solutions employing an extended xenolith data base from other localities in Europe.

7 SUMMARY AND CONCLUSIONS

A combined seismic and petrological model has been derived for the uppermost mantle beneath southern Germany. This model fits the seismic P_n traveltime and amplitude data, the limited amount of mantle xenolith data, and uppermost mantle temperatures derived from surface heat-flow data. The model consists of an anisotropic layer about 10 km thick immediately below the Moho. The *P*-wave velocity immediately below the Moho is about 8.03 km s^{-1} in the fast direction (N31°E) and 7.77 km s^{-1} in the slow direction; the amount of anisotropy is thus about 3–4 per cent. The anisotropy increases with depth as the horizontal *P*-wave velocity–depth gradient in the fast direction is 0.06 s^{-1}, while in the slow direction it is zero. The amount of anisotropy 10 km below the Moho is about 11 per cent. Thus, although the average amount of anisotropy in this 10 km thick layer is approximately the same as that derived by Bamford (1976b, 1977), the distribution of the anisotropy with depth is somewhat different. This is due mainly to the analysis of the P_n amplitudes carried out in the study. The model requires a P_n velocity of 8.63 km s^{-1} in the fast direction at 40 km depth. This velocity is considerably lower than that predicted by Fuchs (1983), which was in excess of 9 km s^{-1} and is in agreement with other velocity estimates in the fast direction at about 40 km depth in southern Germany (Ansorge, Bonjer & Emter 1979). This seismic model requires a petrological model that displays a strong chemical inhomogeneity with depth in the uppermost mantle. Immediately beneath the Moho, olivine-poor harzburgites (57 per cent Ol) should occur with about 20 per cent of the olivine grains being preferentially

oriented. This composition should gradually change with depth until at about 10 km below the Moho, where Ol-rich peridotites (90 per cent Ol) should occur with about 40 per cent of the olivine grains being preferentially oriented.

The reasons for utilizing a 10 km thickness for the anisotropic uppermost mantle layer are now discussed. Based on traveltime analysis of the profiles SB-060 and 09-240, Fuchs (1983) utilized a 10 km thickness for this layer in the anvil model. Models in which the thickness of this layer is about 5–6 km produce maximum amplitude ratios between the P_n and the dominant crustal phase of around 0.5, which is clearly too small (see Figs 9 and 13). For models in which the thickness of this layer is 14–15 km, velocities of around 8.9 km s^{-1} occur at the bottom of the layer in the fast velocity direction. Although velocities of 8.5–8.6 km s^{-1} at about 40 km depth have been reported from southern Germany in the fast velocity direction (Ansorge *et al.* 1979), velocities of 8.9 km s^{-1} have not. Further, it is not possible to find petrological models involving typical mantle minerals using reasonable geotherms for both the top and the bottom of this layer if it is 14–15 km thick and has the velocity distribution described above. Based on the above reasons the thickness of the anisotropic uppermost mantle layer has been chosen to be 10 km in this study, and the possible error in this value is estimated to be $\pm$1–2 km.

The horizontal phase velocities of the new model for the uppermost anisotropic layer are shown in Fig. 17. In addition to the *P*-wave velocities (Fig. 17a) discussed above, the two quasi-*S*-wave velocities (Fig. 17b–c) are shown. The directions of fast and slow *P*-wave velocities are oriented along the *x*- and *y*-axes, respectively, and the model is 10 km thick in the direction of the *z*-axis. Directions in which higher velocity gradients occur are denoted by light shading, while directions in which lower gradients occur are denoted by dark shading. In contrast to the horizontal *P*-wave velocity gradients, the largest quasi-*S*-wave velocity gradients are much smaller. While one of the quasi-*S* waves (*qS*2) also has the largest velocity gradient along the direction of the *x*-axis, the other quasi-*S*-wave (*qS*1) has the largest velocity gradient at 45° to the *x*-axis. The maximum velocity gradient of the *qS*2 wave is about 10 times smaller than the maximum velocity gradient of the *qS*1 wave. Thus, bearing in mind that the direction of fast horizontal *P*-wave velocity in southern Germany is N31°E,

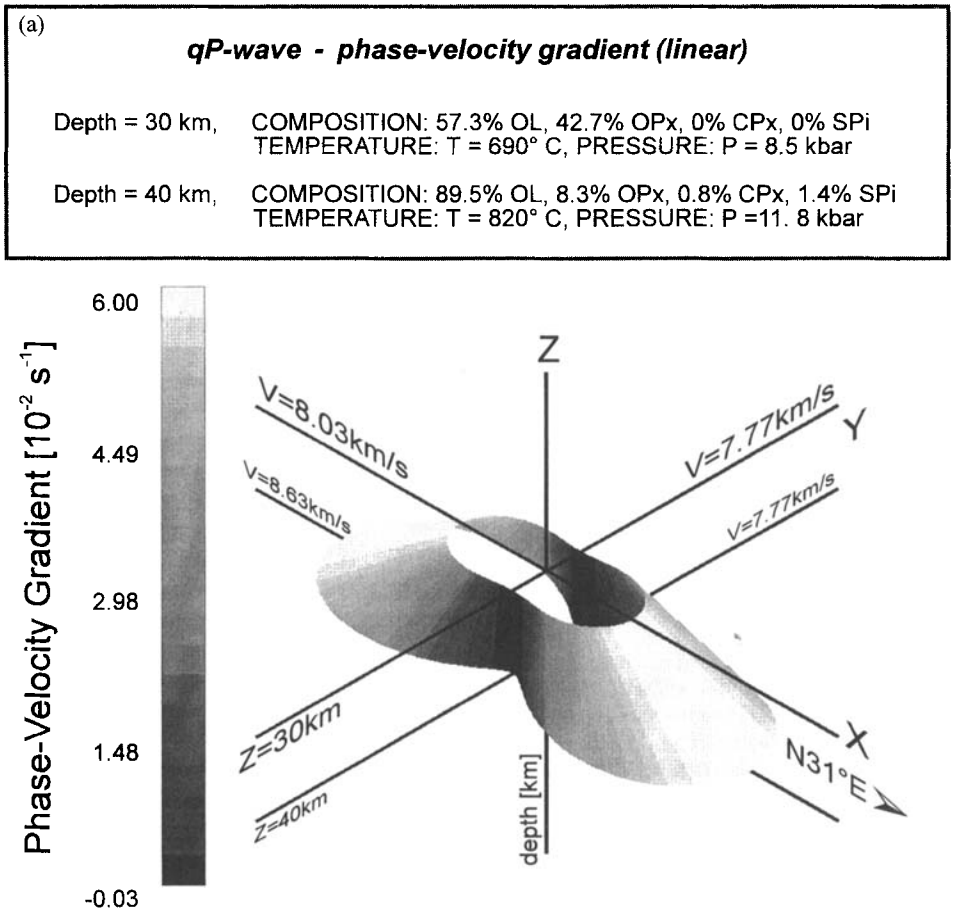

Figure 17. (a) New 3-D model for the horizontal *qP*-wave velocity in the mantle beneath southern Germany between the Moho at 30 km depth and 40 km depth. Directions in which higher velocity gradients occur are denoted by light shading while directions in which lower gradients occur are denoted by dark shading. The azimuth of the *x*-axis beneath southern Germany would be N31°E. (b) New 3-D model for the horizontal *qS*1-wave velocity in the mantle beneath southern Germany between the Moho at 30 km depth and 40 km depth. The *qS*1 wave is the faster *S* wave, which is mainly polarized perpendicular to the sagittal plane. The azimuth of the *x*-axis beneath southern Germany would be N31°E. Note that for this wave type the direction of highest velocity is 45° off the axis of highest *P*-wave velocity (*x*-axis). (c) New 3-D model for the horizontal *qS*2-wave velocity in the mantle beneath southern Germany between the Moho at 30 km depth and 40 km depth. The *qS*2 wave is the slower *S* wave which is mainly polarized parallel to the sagittal plane. The azimuth of the *x*-axis beneath southern Germany would be N31°E.

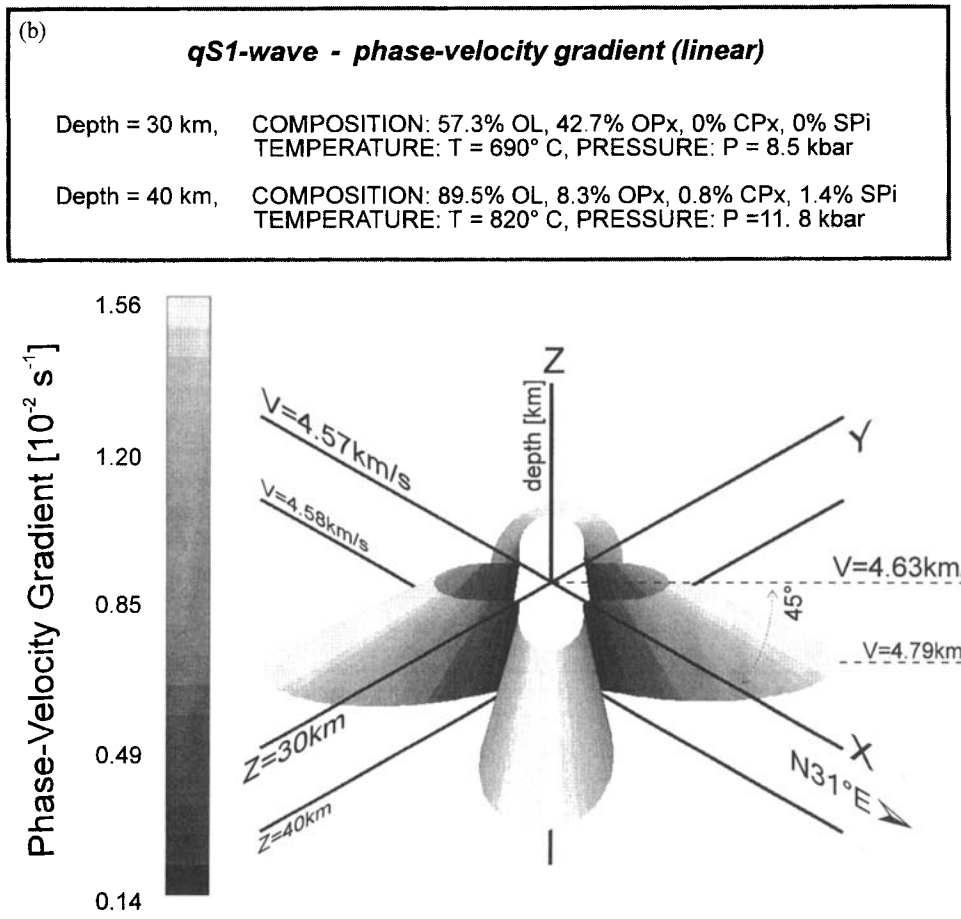

Figure 17. (*Continued.*)

the greatest possibility of detecting S_n amplitudes in southern Germany would be in the directions of about N76°E and N166°E. Record sections derived from local earthquake recordings along these azimuths do show S_n amplitudes (Plenefisch, Faber & Benjer 1994).

It will be necessary to look at deeper-penetrating phases on several profiles to update the lower parts of the anvil model. However, a homogeneous layer some kilometres thick is required below the uppermost gradient layer in order to allow P_n to propagate to far enough distances in the fast direction.

ACKNOWLEDGMENTS

We acknowledge the advice and discussions with our colleagues at the Geophysical Institute, Karlsruhe. The calculations were performed on HP-Workstations, the IBM3090 and the Siemens S600 supercomputer of the computer centre, Karlsruhe University. The visit of SS to Germany was supported by the Alexander von Humboldt Foundation. Geophysical Institute Contribution Number 655.

REFERENCES

Ansorge, J., Bonjer, K.-P. & Emter, D., 1979. Structure of the uppermost mantle from long-range seismic observations in southern Germany and the Rhinegraben area, *Tectonophysics,* **56,** 31–48.

Backus, G.E., 1965. Possible forms of seismic anisotropy of the uppermost mantle under oceans, *J. geophys. Res.,* **70,** 3429–3429.

Bamford, D., 1973. Refraction data in Western Germany—a time-term interpretation, *J. Geophys.,* **39,** 907–927.

Bamford, D., 1976a. MOSAIC time-term analysis, *Geophys. J. R. astr. Soc.,* **44,** 433–446.

Bamford, D., 1976b. An updated time-term interpretation of Pn data for quarry blasts and explosions in Western Germany, in *Explosion seismology in central Europe—data and results,* pp. 215–220, eds Giese, P., Prodehl, C. & Stein, A., Springer-Verlag, Berlin-Heidelberg-New York.

Bamford, D., 1977. P_n anisotropy in a continental upper mantle, *Geophys. J. R. astr. Soc.,* **49,** 29–48.

Berry, M.J., & West, G.F., 1966. An interpretation of the first arrival data of the Lake Superior experiment by the time-term method, *Bull. seism. Soc. Am.,* **56,** 141–171.

Blundell, D., Freeman, R. & Müller, St., 1992. *A continent revealed: the European Geotraverse,* Cambridge University Press, Cambridge.

Booth, D. & Crampin, S., 1983. The anisotropic reflectivity technique: theory, *Geophys. J. R. astr. Soc.,* **72,** 755–766.

Dobrin, M.B., 1976. *Introduction to Geophysical Prospecting,* 3rd edn, McGraw-Hill, New York, NY.

Duffy, T.S. & Anderson, D.L., 1989. Seismic velocities in mantle minerals and the mineralogy of the upper mantle, *J. geophys. Res.,* **94,** 1895–1912.

Edel, J.-B., Fuchs, K., Gelbke, C. & Prodehl, C., 1975. Deep structure of the southern Rhinegraben area from seismic refraction investigations, *J. Geophys.,* **41,** 333–356.

EUGEMI Working Group, 1990. The European Geotraverse seismic refraction experiment of 1986 from Genova, Italy, to Kiel, Germany, *Tectonophysics,* **176,** 43–57.

Fuchs, K., 1983. Recently formed elastic anisotropy and petrological

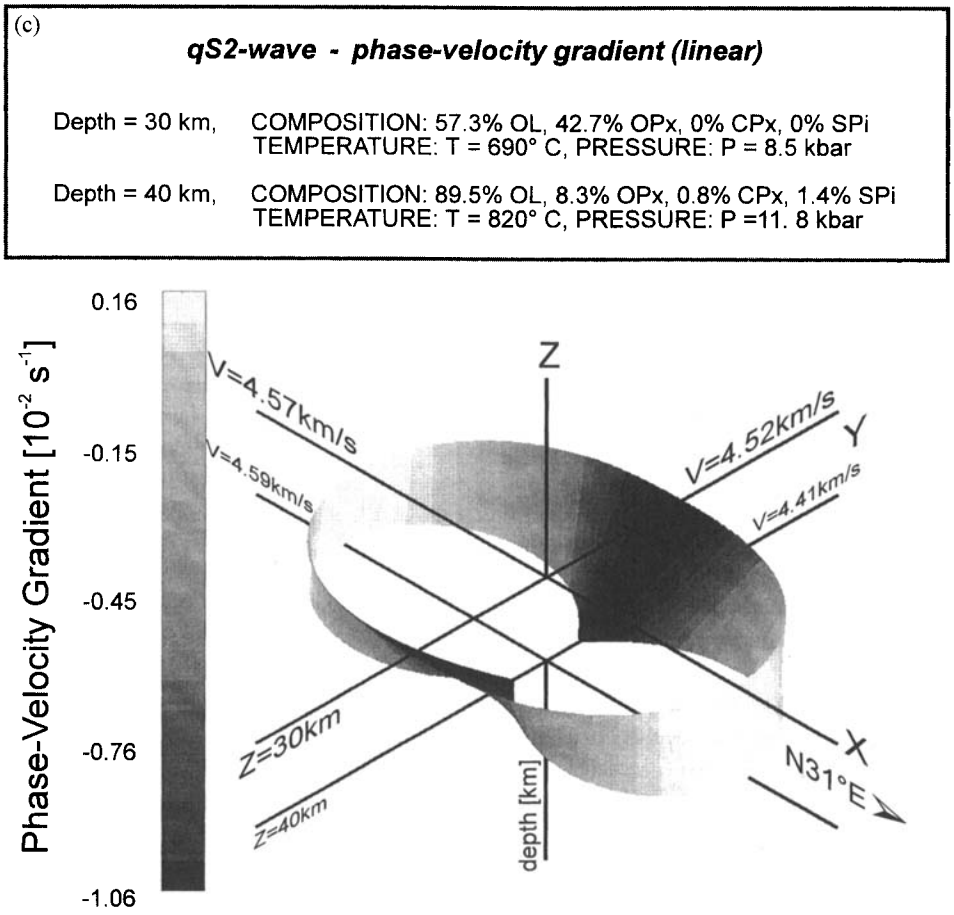

Figure 17. (*Continued.*)

models for the continental subcrustal lithosphere in southern Germany, *Phys. Earth planet. Inter.*, **31,** 93–118.

Gajewski, D. & Prodehl, C., 1985. Crustal structure beneath the Swabian Jura, SW Germany, from seismic refraction investigation, *J. Geophys.*, **56,** 69–80.

Gajewski, D. & Prodehl, C., 1987. Seismic refraction investigation of the Black Forest, *Tectonophysics,* **142,** 27–48.

Geological map of the Federal Republic of Germany 1 : 1 000 000, 1973. Bundesanstalt für Bodenforschung, Hannover.

Giese, P., Prodehl, C. & Stein, A., 1976. *Explosion seismology in central Europe–data and results,* Springer-Verlag, Berlin-Heidelberg-New York.

Hashin, Z. & Shtrikman, S., 1962. A variational approach to the theory of elastic behaviour of polycrystals, *J. Mech. Phys. Solids,* **10,** 343–352.

Hearn, T.M., 1984. Pn travel times in southern California, *J. geophys. Res.,* **89,** 1843–1855.

Isaak, D.G., 1992. High-temperature elasticity of iron-bearing olivines, *J. geophys. Res.,* **97,** 1871–1885.

Kumazawa, M. & Anderson, O.L., 1969. Elastic moduli, pressure derivatives, and temperature derivatives of single-crystal olivine and single-crystal fosterite, *J. geophys. Res.,* **74,** 5311–5320.

Nicolas, A., Bouchez, J.L., Boudier, F. & Mercier, J.C., 1971. Textures, structures and fabrics due to solid-state flow in some European lherzolites, *Tectonophysics,* **12,** 55–86.

Nolte, B., 1988. Erweiterung und Anwendung des Reflektivitäts-programms für anisotrope Medien, *Diploma thesis,* University of Karlsruhe, Germany.

Nolte, B., Frazer, N.L. & Mallik, S., 1992. Seismogram synthesis for azimuthally anisotropic media with a single slowness integration, *Geophys. J. Int.,* **111,** 127–140.

Plenefisch, T., Faber, S. & Bonjer, K.P., 1994. Investigations of S_n and P_n phases in the area of the upper Rhine Graben and northern Switzerland, *Geophys. J. Int.,* **119,** 402–420.

Pollack, H.N. & Chapman, D.S., 1977. On the regional variation of heat flow, geotherms and lithospheric thickness, *Tectonophysics,* **38,** 279–296.

Raitt, R.W., Shor, G.G., Francis, T.J.G. & Morris, G.B., 1969. Anisotropy of the Pacific upper mantle, *J. geophys. Res.,* **74,** 3095–3109.

Sachs, P.M., 1988. Untersuchungen zum Stoffbestand der tieferen Lithosphäre an Xenolithen südwestdeutscher Vulkane, *PhD thesis,* Geophysikalisches Institut, University of Karlsruhe, Germany.

Smith, T.J., Steinhart, J.S. & Aldrich, L.T., 1966. Lake Superior crustal structure, *J. geophys. Res.,* **71,** 1141–1172.

Sobolev, S. & Babeyko, A., 1994. Modeling of mineralogical composition, density and elastic wave velocities in anhydrous magmatic rocks, *Surveys Geophys.,* **15,** 515–544.

Willmore, P.L. & Bancroft, A.M., 1960. The time-term approach to refraction seismology, *Geophys. J. R. astr. Soc.,* **3,** 419–432.

Zeis, St., Gajewski, D. & Prodehl, C., 1990. Crustal structure of southern Germany from seismic refraction data, *Tectonophysics,* **176,** 59–86.

Zervas, Ch.E. & Crosson, R.S., 1986. Pn observation and interpretation in Washington, *Bull. seism. Soc. Am.,* **76,** 521–546.